

Parameterisations of thermal bomb explosions for core-collapse supernovae and ^{56}Ni production

Liliya Imasheva,^{1,2*} Hans-Thomas Janka,^{1,3} and Achim Weiss^{1,2}

¹*Max-Planck Institut für Astrophysik, Karl-Schwarzschild-Str. 1, 85748 Garching, Germany*

²*Ludwig-Maximilians-Universität München, Geschwister-Scholl-Platz 1, 80539 Munich, Germany*

³*Physik-Department, Technische Universität München, James-Franck-Str. 1, 85748 Garching, Germany*

Accepted XXX. Received YYY; in original form ZZZ

ABSTRACT

Thermal bombs are a widely used method to artificially trigger explosions of core-collapse supernovae (CCSNe) to determine their nucleosynthesis or ejecta and remnant properties. Recently, their use in spherically symmetric (1D) hydrodynamic simulations led to the result that $^{56,57}\text{Ni}$ and ^{44}Ti are massively underproduced compared to observational estimates for Supernova 1987A, if the explosions are slow, i.e., if the explosion mechanism of CCSNe releases the explosion energy on long timescales. It was concluded that rapid explosions are required to match observed abundances, i.e., the explosion mechanism must provide the CCSN energy nearly instantaneously on timescales of some ten to order 100 ms. This result, if valid, would disfavor the neutrino-heating mechanism, which releases the CCSN energy on timescales of seconds. Here, we demonstrate by 1D hydrodynamic simulations and nucleosynthetic post-processing that these conclusions are a consequence of disregarding the initial collapse of the stellar core in the thermal-bomb modelling before the bomb releases the explosion energy. We demonstrate that the anti-correlation of ^{56}Ni yield and energy-injection timescale vanishes when the initial collapse is included and that it can even be reversed, i.e., more ^{56}Ni is made by slower explosions, when the collapse proceeds to small radii similar to those where neutrino heating takes place in CCSNe. We also show that the ^{56}Ni production in thermal-bomb explosions is sensitive to the chosen mass cut and that a fixed mass layer or fixed volume for the energy deposition cause only secondary differences. Moreover, we propose a most appropriate setup for thermal bombs.

Key words: nuclear reactions, nucleosynthesis, abundances – supernovae: general – hydrodynamics

1 INTRODUCTION

Core-collapse supernovae (CCSNe) are one of the primary sources of heavy elements in the universe. They modify and disseminate the products of the nucleosynthesis of their massive stellar progenitors and freshly produce radioactive and trans-iron species through various processes such as explosive burning in the shock-heated ejecta, freeze-out from nuclear statistical equilibrium, neutrino-induced reactions, and neutron and proton capture chains (e.g., Woosley et al. 2002; Sukhbold et al. 2016; Curtis et al. 2019; Ebinger et al. 2020; Cowan et al. 2021; Diehl et al. 2021). Thus they play a crucial role as one of the main drivers of galactic chemical evolution (e.g., Timmes et al. 1995; Matteucci 2003; Hayden et al. 2015; Kobayashi et al. 2020; Wirth et al. 2021).

Large sets of progenitor models need to be surveyed with numerical simulations of CCSNe in order to account for a rich diversity of pre-collapse conditions, because the evolution of massive stars depends not only on the stellar mass and metallicity but also on the amount of rotation and the

strength of internal magnetic fields, different prescriptions of mass loss rates through stellar winds as well as binary interactions and mergers. Moreover, uncertainties connected to nuclear rates and the treatment of multi-dimensional effects such as angular momentum transport, convection, overshooting, and boundary mixing cause variations. Systematic investigations of large model sets are therefore indispensable for characterising the electromagnetic signatures of CCSNe linked to different types of hydrogen-rich and stripped progenitors (e.g., Sukhbold et al. 2016; Dessart et al. 2021a; Ricks & Dwarkadas 2019; Dessart et al. 2021b; Curtis et al. 2021; Barker et al. 2022). The same effort is also necessary for predicting the mass distributions of neutron stars and black holes as the compact remnants of stellar core collapse events (e.g., Ugliano et al. 2012; Pejcha & Thompson 2015; Sukhbold et al. 2016; Müller et al. 2016; Ebinger et al. 2019; Ertl et al. 2020; Woosley et al. 2020; Schneider et al. 2021; Meskhi et al. 2022), which are responsible for the growing repository of measured gravitational-wave signals when they are components in close binary systems (Abbott et al. 2021; The LIGO Scientific Collaboration et al. 2021).

Although the mechanisms of CCSN explosions, either

* E-mail: imasheva@mpa-garching.mpg.de

neutrino-driven or magneto-rotational, have been recognized to be generically multi-dimensional hydrodynamic phenomena (see, e.g., Woosley & Janka 2005; Janka et al. 2007; Mezzacappa 2005; Janka 2012; Hix et al. 2014; Janka et al. 2016; Müller 2016; Couch 2017; Müller 2020; Burrows & Vartanyan 2021, for reviews of full-fledged state-of-the-art, multi-dimensional CCSN simulations), three-dimensional (3D) simulations are still constrained by their prohibitive requirements of computational resources. Therefore the enormous diversity of the progenitor conditions can currently be accounted for only by CCSN calculations in spherical symmetry (one dimension; 1D), which permit to follow the long-time evolution in order to determine the explosion properties including nucleosynthesis and electromagnetic observables for large sets of stellar models.

Traditionally, this task has been undertaken by triggering the CCSN explosions artificially either by a so-called “thermal bomb” mechanism (e.g., Shigeyama et al. 1988; Hashimoto et al. 1989; Thielemann et al. 1990, 1996; Nakamura et al. 2001; Nomoto et al. 2006; Umeda & Nomoto 2008; Moriya et al. 2010; Bersten et al. 2011), in which an outgoing shock wave is initiated by dumping thermal energy into a chosen volume around a chosen initial mass cut. This initial mass cut is picked by nucleosynthesis constraints based on the electron fraction (Y_e) of the pre-collapse progenitor or by guessing the mass of the compact remnant, and it is intended to define the borderline between this emerging compact object and the explosion ejecta before fallback happens later and possibly brings back matter that does not achieve to become gravitationally unbound. Or, alternatively, the outgoing shock was generated by a piston-driven mechanism (e.g., Woosley 1988; Woosley & Weaver 1995; Woosley et al. 2002; Woosley & Heger 2007; Zhang et al. 2008), where kinetic energy is deposited by the outward motion of a piston, which is placed at a chosen Lagrangian mass shell corresponding to the initial mass cut to push the overlying shells. Refinements of these methods concern, for example, a contraction of the location of the piston or initial mass cut to mimic the collapse that precedes the subsequent expansion, and variations of the duration of the energy deposition by the thermal bomb instead of an instantaneous delivery of the energy. In yet another approach (e.g., Limongi & Chieffi 2003, 2006, 2012; Chieffi & Limongi 2013; Limongi & Chieffi 2018) a “kinetic bomb” approach was applied in 1D Lagrangian hydrodynamic simulations of CCSN explosions such that the blast wave is started by imparting an initial expansion velocity at a mass coordinate around $1 M_\odot$, which is still well inside the iron core, and tuning the value of this velocity such that desired values of the ejected amount of ^{56}Ni and/or of the final kinetic energy of the ejecta are obtained. Also multi-dimensional (2D, 3D) variants of the method of thermal (or kinetic) bombs exist to trigger highly asymmetric blast waves and jet-induced or jet-associated explosions (see, e.g., Nagataki et al. 1997; MacFadyen & Woosley 1999; Khokhlov et al. 1999; Aloy et al. 2000; Nagataki et al. 2003; Maeda & Nomoto 2003; Nagataki et al. 2006; Ono et al. 2020; Orlando et al. 2020, for a few exemplary applications from a rich spectrum of publications).

All of these methods of artificially exploding massive stars depend on numerous free parameters, for example the location of the initial mass cut, the width of the energy-deposition region and the timescale of energy deposition for the thermal bomb, the duration and depth of the collapse-like contrac-

tion, and the initial expansion velocity and coasting radius for the piston method, the initial velocity of the kinetic bomb, or the 2D/3D geometry of the energy input. These parameters are chosen suitably to produce defined values for the explosion energy and the expelled ^{56}Ni mass or to reproduce multi-dimensional properties of observed supernovae and supernova remnants. Such degrees of freedom have an influence on the nucleosynthetic yields through the initial strength of the shock and the volume and extent of the heating achieved by the thermal energy injection, which determine the ejecta mass where sufficiently high peak temperatures for nuclear reactions are reached. Moreover, the traditional explosion recipes do not enable one to track the conditions in the innermost ejecta, whose neutron-to-proton ratio gets reset by the exposure to the intense neutrino fluxes from the nascent neutron star or from an accretion torus around a new-born black hole (see, e.g., Bruenn et al. 2016; Müller et al. 2017a; Siegel et al. 2019; Bollig et al. 2021).

For these reasons more modern CCSN explosion treatments by means of “neutrino engines” have been introduced that attempt to capture essential effects of the neutrino-driven mechanism but replace the highly complex and computationally intense, energy and direction dependent neutrino transport used in full-fledged neutrino-hydrodynamical CCSN models by simpler treatments. This line of research has been pursued in 2D and 3D simulations either neglecting neutrino transport and replacing it by a so-called light-bulb approximation with chosen (time-dependent) neutrino luminosities and spectra (e.g., Janka & Müller 1996; Kifonidis et al. 2000; Shimizu et al. 2001; Kifonidis et al. 2003, 2006; Yamamoto et al. 2013) or by using an approximate, grey description of the neutrino transport with a boundary condition for the neutrino emission leaving the optically thick, high-density core of the proto-neutron star (e.g., Scheck et al. 2006; Wongwathanarat et al. 2010, 2013, 2015, 2017).

Neutrino-engine treatments are also applied in 1D hydrodynamic CCSN simulations with neutrino transport schemes of different levels of refinement for determining the supernova and compact remnant properties as well as the associated nucleosynthetic outputs for large sets of stellar progenitor models. In these studies neutrino-driven explosions are obtained by parametrically increasing the neutrino-energy deposition behind the stalled bounce shock (O’Connor & Ott 2011), by describing the neutrino emission of the newly formed neutron star via a model with parameters that are calibrated to reproduce basic properties of the well-observed CCSNe of SN 1987A and SN 1054 (Crab) (P-HOTB; Ugliano et al. 2012; Ertl et al. 2016; Sukhbold et al. 2016; Ertl et al. 2020), by parametrizing additional energy transfer to the CCSN shock via muon and tau neutrinos (also using observational constraints) (PUSH; Perego et al. 2015; Ebinger et al. 2019; Curtis et al. 2019; Ebinger et al. 2020), or by also including the effects of convection and turbulence through a modified mixing-length theory approach with free parameters adjusted to fit the results of 3D simulations (STIR; Couch et al. 2020). Alternatively to these novel simulation approaches, semi-analytic descriptions have been applied, either by using spherical, quasi-static evolutionary sequences to determine the explosion threshold and energy input to the explosion via a neutrino-driven wind (Pejcha & Thompson 2015) or by parametrically phrasing the elements of multi-dimensional processes that play a role in initiating and powering CC-

SNe via the neutrino-heating mechanism (Müller et al. 2016; Schneider et al. 2021; Aguilera-Dena et al. 2022).

Despite these more advanced modelling efforts, which generally reflect more of the physics of the CCSN explosion mechanism than thermal-bomb or piston models, the latter are still widely used. In fact, thermal bombs have experienced an increase in popularity in 1D applications recently, because they are applied in the open-source codes MESA (Paxton et al. 2011, 2015) and SNEC (Morozova et al. 2015). They have the advantage of simplicity and great flexibility in their usage, allowing one to control the dynamics of the explosion by choosing the value, timescale, mass layer or volume of the energy deposition, and the evolution of the inner boundary, i.e., if and how the collapse of the stellar core is taken into account.

The sensitivities of the traditional thermal or kinetic bombs and piston mechanisms and of the associated nucleosynthesis to the involved parameterisations and the corresponding limitations of these methods have been investigated in previous works, though never comprehensively (Aufderheide et al. 1991; Young & Fryer 2007). In a seminal study Aufderheide et al. (1991) discussed the parameters employed in the numerical recipes to artificially launch the explosion of a $20 M_{\odot}$ progenitor in 1D. They initiated explosions at different locations of enclosed mass, and compared the ejecta conditions (especially the peak temperatures reached behind the outgoing shocks) as well as the explosively created nuclear yields. In particular, they considered thermal bomb and piston calculations for two variations, namely when the inner core was allowed to collapse prior to shock initiation or not. We will call such cases “collapsed” (C) versus “uncollapsed” (U) models. They concluded that the former are a better representation of the CCSN physics, which is governed by the iron-core collapse to a neutron star. However, in their study the C-cases also showed more differences between piston and bomb results. Their main concerns were the uncertainties in the choice of the mass-cut location and in the assumed duration of the initial collapse phase, and the differences in the peak temperature because of too much kinetic energy being connected to the piston and too much thermal energy to the bomb mechanism. Moreover, they expressed concerns that the instantaneous energy deposition assumed in their simulations might not be appropriate if the CCSN mechanism is delayed and the shock receives energy input by neutrino heating for several seconds (as indeed seen in state-of-the-art self-consistent CCSN simulations, e.g., Bollig et al. 2021).

In a subsequent study, Young & Fryer (2007) arrived at similar conclusions and found not only a strong sensitivity of the elemental and isotopic yields of silicon and heavier elements to the assumed explosion energy, but also considerable differences of the abundances of these nuclei between piston-driven and thermal-bomb type explosions even for the same explosion energy. In particular, they considered a $23 M_{\odot}$ star, whose collapse, bounce-shock formation, and shock stagnation were followed by a 1D neutrino-hydrodynamics simulation. Their work was focused on triggering explosions of different energies by thermal energy injection over time intervals of 20 ms, 200 ms, and 700 ms, starting at 130 ms after bounce (corresponding to 380 ms after the start of the collapse simulation) and leading to explosions at 150 ms, 330 ms, and 830 ms after bounce, respectively. The authors reported a considerable increase of intermediate-mass and Fe-group

yields with the longer delay times of the explosion (i.e., longer duration of the energy deposition) and, in particular significantly more (orders of magnitude!) ^{56}Ni and several times more ^{44}Ti production for models with 1.5×10^{51} erg explosion energy and 200 ms and 700 ms delay time compared to a case with the same explosion energy but a short energy injection time of only 20 ms.

Recently, Sawada & Maeda (2019) (in the following SM19) published a study where they came to exactly the opposite conclusion based on 1D hydrodynamic CCSN models with a thermal-bomb prescription to trigger the explosions of 15, 20, and $25 M_{\odot}$ progenitors. They found that the produced amount of ^{56}Ni decreases with longer timescales of the energy deposition; observational constraints for nucleosynthesis products of CCSNe could be fulfilled only by rapid explosions when the final blast-wave energy was reached within $\lesssim 250$ ms, and best compatibility was obtained for nearly instantaneous explosions where the energy was transferred within $\lesssim 50$ ms. They interpreted their results as a serious challenge for the neutrino-heating mechanism, which delivers the explosion energy in progenitors as massive as those considered by SM19 only on timescales that are significantly longer than 1 s (see Bruenn et al. 2016; Müller et al. 2017a; Bollig et al. 2021; Burrows & Vartanyan 2021).

However, the opposite trends reported by Young & Fryer (2007) and SM19 for the dependence of the ^{56}Ni yields on the energy-deposition timescale do not need to contradict each other. In this context it is important to remember that the former study considered collapsed (C) models, whereas SM19 did not collapse their stars (using U models) before switching on the thermal energy deposition. This is likely to have important consequences for the hydrodynamic response of the stellar gas when the energy input happens on different timescales. With the expansion of the heated gas setting in, which is easier in an uncollapsed star, expansion cooling takes place. Therefore slow energy injection in a star that has not collapsed will not be able to achieve sufficiently high temperatures in sufficiently large amounts of ejecta to enable any abundant production of ^{56}Ni .

In our work we aim at investigating this question quantitatively by means of 1D hydrodynamical simulations within the framework of the thermal-bomb method. Two different aspects serve us as motivation. First, SM19 and also Suwa et al. (2019) claimed that long energy transfer timescales or slow growth rates of the blast-wave energy (“slow explosions”) suppress the ^{56}Ni production. The authors interpreted this proposition as a problem for current self-consistent neutrino-driven explosion models and the neutrino-driven mechanism itself. Second, our study is supposed to assist the design of suitable thermal-bomb treatments that can serve as easy-to-implement methods to conduct systematic CCSN simulations in 1D for large progenitor sets without the need of a detailed treatment of neutrinos. Naturally, such approaches can never capture all aspects of “realistic” multi-dimensional CCSN models, in particular not with regard to the innermost, neutrino-processed ejecta. Nevertheless, such simplified explosion treatments can still be useful to answer many observationally relevant questions, in particular since the explosive nucleosynthesis past the outer edge of the silicon shell is mostly determined by the explosion energy and the progenitor structure, but little sensitive to the initiation method of

the explosion (Aufderheide et al. 1991).¹ Similarly, the explosive nucleosynthesis in these layers is also unlikely to depend strongly on the neutrino physics and the multi-dimensional hydrodynamic processes that play a crucial role in the CCSN mechanism and that determine the observable asymmetries of the explosions.

In this paper we thus investigate the influence of the energy-deposition timescale for thermal bombs in collapsed as well as uncollapsed models. But instead of conducting a complete survey of all free parameters needed to steer the thermal bombs, we will stick to simple and well-tested prescriptions already applied in previous publications. For a diagnostic property we will focus on the produced mass of ^{56}Ni before any effects of fallback could modify the ejecta, because fallback will also depend on the radially outward mixing of metals and thus on multi-dimensional effects that can be accounted for in 1D models only with additional assumptions for parametric treatments. The amount of ^{56}Ni produced by the CCSN “engine” is not only a crucial characteristic of the early dynamics of the explosion but also a primary observable that governs the light curve and the electromagnetic display of CCSNe from weeks to many years (e.g. Arnett et al. 1989; Iwamoto et al. 1994). In a follow-up paper we plan to explore a wider range of thermal-bomb parameterisations and check them against piston-triggered and neutrino-driven CCSN explosion models. Moreover, in this subsequent work we will compare the results for a greater selection of products of explosive nucleosynthesis.

Our paper is organised as follows. In Section 2 we briefly describe the stellar evolution models considered in our study, the methodology of the hydrodynamic explosion modelling, the small nuclear reaction network used in the hydrodynamic simulations and the large network applied in a more detailed post-processing of the nucleosynthesis. In Section 3 we describe our setup for reference models, guided by the calculations reported by SM19, i.e., uncollapsed models, as well as the variations investigated by us, i.e., collapsed models and different mass layers vs. radial volumes for the energy deposition. In Section 4 we present our results, followed by a summary and discussion in Section 5.

2 METHODS AND INPUTS

In this section we describe the three aspects of our calculations: the progenitors used as input models, the corresponding explosion simulations including the definition of the thermal bomb method, and the nucleosynthetic post-processing with an extended nuclear-reaction network. Our progenitors were taken from the work of Sukhbold & Woosley (2014), the explosion modelling was performed using the hydrodynamic code PROMETHEUS-HOTB (Janka & Müller 1996; Kifonidis et al. 2003; Scheck et al. 2006; Arcones et al. 2007; Ugliano et al. 2012; Ertl et al. 2016), but without making use of the neutrino-transport module associated with this code, and the detailed explosive nucleosynthesis was calculated with the SkyNet open-source nuclear network code (Lippuner & Roberts 2017).

¹ According to present-day understanding, this statement better holds good for the outer edge of the oxygen layer instead of the silicon shell.

Table 1. Properties of the progenitors used in this work. M_{pre} is the total pre-collapse mass, M_{He} is the mass of the helium core, M_{CO} the mass of CO core, $M_{s=4}$ is the enclosed mass where the dimensionless entropy $s/k_{\text{B}} = 4$, and $M_{Y_e=0.48}$ is the enclosed mass where the electron fraction is equal to 0.48. All the masses are in M_{\odot} .

M_{ZAMS}	M_{pre}	M_{He}	M_{CO}	$M_{s=4}$	$M_{Y_e=0.48}$
12.3	11.0599	3.29162	2.22902	1.59102	1.23017
19.7	15.7490	6.09592	4.85410	1.53298	1.25635
21.0	16.1109	6.62284	5.37384	1.48435	1.27209
26.6	15.3093	8.96794	7.69495	1.73833	1.38264

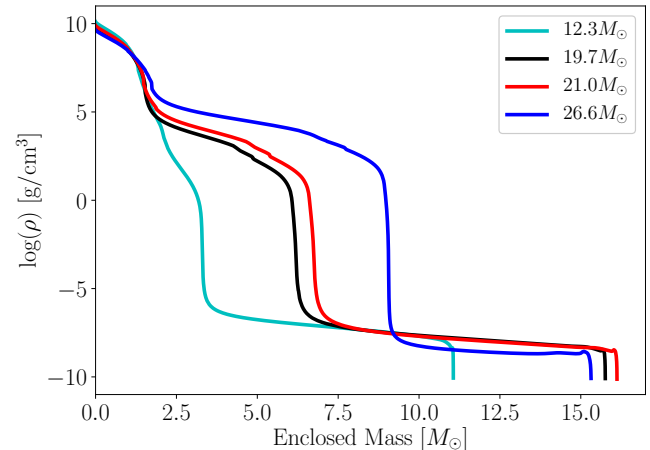


Figure 1. Density structure as a function of enclosed mass for the considered progenitors with $M_{\text{ZAMS}} = 12.3 M_{\odot}$ (cyan line), $19.7 M_{\odot}$ (black line), $21.0 M_{\odot}$ (red line), and $26.6 M_{\odot}$ (blue line). The color convention for the progenitors is kept the same throughout our paper.

2.1 Presupernova models

The progenitor models for this work were computed with the 1D hydrodynamics code KEPLER (Weaver et al. 1978) and are a subset of the large model set published by Sukhbold & Woosley (2014). They represent non-rotating stars with solar metallicity, which were evolved from the main sequence until the onset of the iron-core collapse. The physics of this set of progenitors was discussed in detail in the literature (e.g. Woosley et al. 2002; Woosley & Heger 2007).

In order to investigate basic features of the nickel production using different setups for the thermal bomb triggering the CCSN explosion, we selected four progenitors with zero-age-main-sequence (ZAMS) masses of $M_{\text{ZAMS}} = 12.3, 19.7, 21.0,$ and $26.6 M_{\odot}$. Their characteristic properties are listed in Table 1, where M_{pre} is the total pre-collapse mass, M_{He} is the helium-core mass defined by the mass coordinate where $X(\text{H}) \leq 0.2$, M_{CO} is the mass of the carbon-oxygen core associated with the location where $X(\text{He}) \leq 0.2$, $M_{s=4}$ is the mass enclosed by the radius where the value of the dimensionless entropy per nucleon is $s/k_{\text{B}} = 4$ (where k_{B} is the Boltzmann constant), and $M_{Y_e=0.48}$ is the enclosed mass where the electron fraction is $Y_e = 0.48$.

This selection of the progenitors is motivated by the aim to cover approximately the same range of progenitor masses as considered by SM19. For the lighter progenitors, we in-

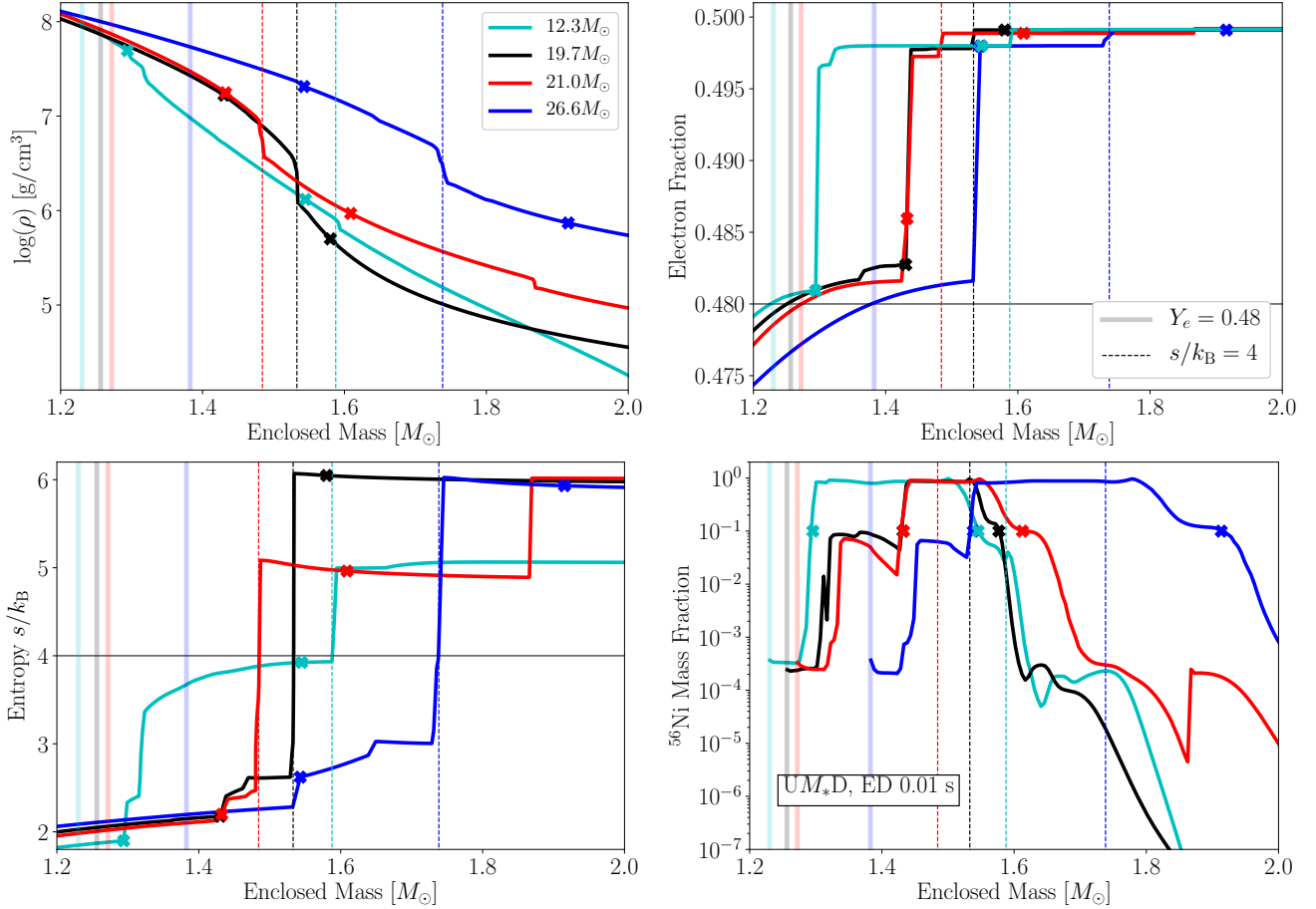


Figure 2. Pre-collapse structure of the progenitors used in this work, namely the density (top left), the dimensionless entropy per nucleon s/k_B (bottom left), and the electron fraction Y_e (top right) versus enclosed mass. Vertical lines indicate the inner grid boundaries chosen in our explosion simulations, with the line colors corresponding to the colors chosen for the four stellar models: the pale solid lines mark the deeper locations where $Y_e = 0.48$, which is also indicated by the horizontal black line in the Y_e plot, and the short-dashed lines define the points where the dimensionless entropy per nucleon s/k_B equals 4, which can also be seen by the horizontal black line in the s/k_B plot. The lower right panel displays the mass fraction of ^{56}Ni obtained as function of enclosed mass for our default setup of uncollapsed models with deep inner boundary; the energy-deposition (ED) timescale assumed for the displayed case is $t_{\text{inj}} = 0.01$ s. The crosses on the stellar profiles in all panels mark the locations of the inner and outer edges of the main production region of ^{56}Ni (see Section 2.1 for the definition of this region). Note that due to the similarity of the profiles the red and black crosses in the two left panels and the lower right panel partly overlap.

investigated two models with $M_{\text{ZAMS}} = 12.3 M_{\odot}$ and $19.7 M_{\odot}$, representing two extreme cases with respect to their density declines at mass coordinates $m \gtrsim 1.5 M_{\odot}$ and differing from each other by the shape of their corresponding density profiles (see Figures 1 and 2). Our simulations are intended to explore the uncertainties in the thermal-bomb modelling, and these progenitor models exhibit a different behavior in the explosive nickel production based on their structure and our calculations, as will be discussed in Section 4.

The upper two panels and the lower left one in Figure 2 visualize the progenitor structures in more details by showing density, electron fraction Y_e , and dimensionless entropy per nucleon as functions of enclosed mass. The crosses indicate the inner and outer edges of the regions where most of the ^{56}Ni is produced, based on the results given in the lower right panel of Figure 2. This last panel displays, as an exemplary case, the nickel mass fractions for one of our setups (namely the uncollapsed models with deep inner boundary and an energy deposition timescale of 0.01 s, see below). The main

region of ^{56}Ni production is defined by the requirement that the mass fraction of this isotope is greater than 0.1 and consequently at least 90% of its total yield are produced between the limits marked by two crosses.

Nickel and other heavy elements are mainly produced in the close vicinity of the inner grid boundaries of the simulations (for the relevant models these are marked by vertical pale solid lines in Figure 2), i.e., close to the mass region that is assumed to end up in the newly formed neutron star. Therefore differences in the ^{56}Ni production will be connected to differences in the progenitor structures between the inner grid boundary and below roughly $2 M_{\odot}$.

2.2 Hydrodynamic explosion modelling

The progenitor models were exploded by making use of the 1D hydrodynamics code PROMETHEUS-HOTB, or in short P-HOTB, which solves the hydrodynamics of a stellar plasma

including evolution equations for the electron fraction and the nuclear species in a conservative manner on an Eulerian grid, employing a higher-order Godunov scheme with an exact Riemann solver. The code employs a micro-physical model of the equation of state that includes a combination of non-relativistic Boltzmann gases for nucleons and nuclei, arbitrarily degenerate and arbitrarily relativistic electrons and positrons, and energy and pressure contributions from trapped photons. Although the hydrodynamics is treated in the Newtonian limit, the self-gravity of the stellar matter takes into account general relativistic corrections. Relevant details of the code and its upgrades over time can be found in the papers of [Janka & Müller \(1996\)](#); [Kifonidis et al. \(2003\)](#); [Scheck et al. \(2006\)](#); [Arcones et al. \(2007\)](#); [Ugliano et al. \(2012\)](#); [Ertl et al. \(2016, 2020\)](#). The CCSN models discussed in this paper were computed with a radial mesh of 2000 zones, geometrically distributed from the inner grid boundary at radius R_{ib} to the stellar surface with a resolution of $\Delta r/R_{\text{ib}} = 10^{-3}$ in the innermost grid cell and $\Delta r/r < 0.013$ everywhere on the grid.

The central volume ($r < R_{\text{ib}}$) was excluded from the computational mesh and replaced by an inner grid boundary at R_{ib} plus a gravitating point mass at the grid center. This introduces a first parameter into the artificial explosion modelling, namely the enclosed mass at the location of this inner boundary (sometimes called the (initial) mass cut), which is identified with the initial mass of the compact remnant. In our calculations we considered two cases for the choice of the position of the inner boundary. In a first case, following SM19, it was placed where $Y_e = 0.48$ in the outer regions of the progenitor’s iron core. This deep location, indicated by the letter “D” in the names of the corresponding explosion models, is extreme because the ejection of matter with Y_e as low as 0.48 is severely constrained by observational bounds on the ^{58}Ni production in CCSNe (see, e.g., SM19 and [Jerstrand et al. 2015](#)). In a second case we placed the inner grid boundary at the location where the dimensionless entropy per nucleon rises to $s/k_B = 4$, which corresponds to the base of the oxygen shell. This position is thus farther out in mass (see Table 1) and is indicated by the letter “O” in the names of the corresponding explosion simulations. This location was also used in 1D piston-driven CCSN models by [Woosley & Heger \(2007\)](#) and [Zhang et al. \(2008\)](#) and is better compatible with the initial mass cut developing in neutrino-driven explosions (see, e.g., [Ertl et al. 2016](#)). In Figure 2 these two choices of the inner boundary position are indicated by vertical lines for each progenitor. Realistically, the surface of the proto-neutron star is likely to be located somewhere between these two positions and will also be determined only after possible fallback has taken place. The mass of the proto-neutron star cannot be significantly larger than the base of the oxygen shell (“O” location), because otherwise the typical neutron star masses will be too big to be compatible with observations ([Woosley & Heger 2007](#)).

The temporal behavior of the inner boundary is likely to affect the dynamics of the explosion, because the effect of the deposition of energy by the thermal-bomb method will depend on the state of the matter the energy is transferred to. If the boundary radius was kept constant at its initial value, i.e., if the stellar core was not collapsed and the explosion was initiated right away, this corresponds to uncollapsed models and is denoted by the initial letter “U” in the model names.

Table 2. Nuclear species used for the nucleosynthetic post-processing of our thermal-bomb CCSN models with SkyNet.

Nuclei used in the 262-species network				
n	1–3H	3–4,6,8He	6–8Li	7,9–12Be
8,10–13B	11–15C	12–16N	13–21O	16–23F
17–24Ne	19–25Na	22–27Mg	25–28Al	27–33Si
29–34P	31–37S	33–38Cl	35–41Ar	37–44K
39–49Ca	43–51Sc	43–54Ti	46–56V	47–58Cr
50–59Mn	51–66Fe	53–67Co	55–68Ni	57–66Cu
58–66Zn	59–67Ga	60–69Ge		

Alternatively, if the boundary was first contracted to mimic the collapse of the progenitor’s degenerate core, this allowed the matter just exterior to the inner boundary to move to the higher densities and deeper into the gravitational potential of the central mass before the bomb was started. This approach defines our collapsed models and is indicated by the initial letter “C” in the names of the corresponding explosion models.

In the thermal bomb method, the CCSN explosion is triggered by thermal energy input into a chosen layer around the inner boundary, either instantaneously (e.g. [Aufderheide et al. 1991](#)) or over a chosen interval in time (e.g., SM19 and [Young & Fryer 2007](#)). The injected energy E_{inj} , the mass layer ΔM or volume ΔV where the energy is deposited, and the timescale of the energy injection t_{inj} are free parameters of such a procedure. These parameters define energy transfer rates per unit of mass or volume, respectively:

$$\dot{e}_{\text{inj},M} = \frac{E_{\text{inj}}}{\Delta M t_{\text{inj}}}, \quad (1)$$

$$\dot{e}_{\text{inj},V} = \frac{E_{\text{inj}}}{\Delta V t_{\text{inj}}}. \quad (2)$$

The expressions of Equations (1) and (2) assume that, for simplicity, the energy input rate is constant in time and thus the deposited energy grows linearly with time.

The total injected energy E_{inj} was varied in order to obtain a chosen value for the terminal explosion energy E_{exp} at infinity. In our study we considered CCSN models with an explosion energy close to $E_{\text{exp}} = 10^{51}$ erg and determined this value at $t \geq 80$ s, at which time it had saturated in each model. The layer of the energy deposition is characterized by two fixed Lagrangian mass coordinates in the case of ΔM and two fixed radii in the case of ΔV . In our simulations the inner boundary of the energy-deposition layer (IBED) was set to be the inner boundary of the computational grid, and the outer boundary of the energy-deposition layer (OBED) depends on the choice of ΔM or ΔV . The last parameter here is the timescale of the energy deposition t_{inj} , which defines how fast the shock will be developing and which we varied in our study, following SM19.

During the CCSN simulations carried out for our investigation, we employed a reflecting inner boundary condition in order to maintain the pressure support while the explosion was still developing. This setting is motivated by the continued push of the CCSN “engine” (either neutrino-driven or magneto-rotational) over the period of time when the blast-wave energy builds up. We note in passing that we do not intend to discuss any effects of fallback, which typically play a role only on timescales longer than those considered for nucleosynthesis in the present work.

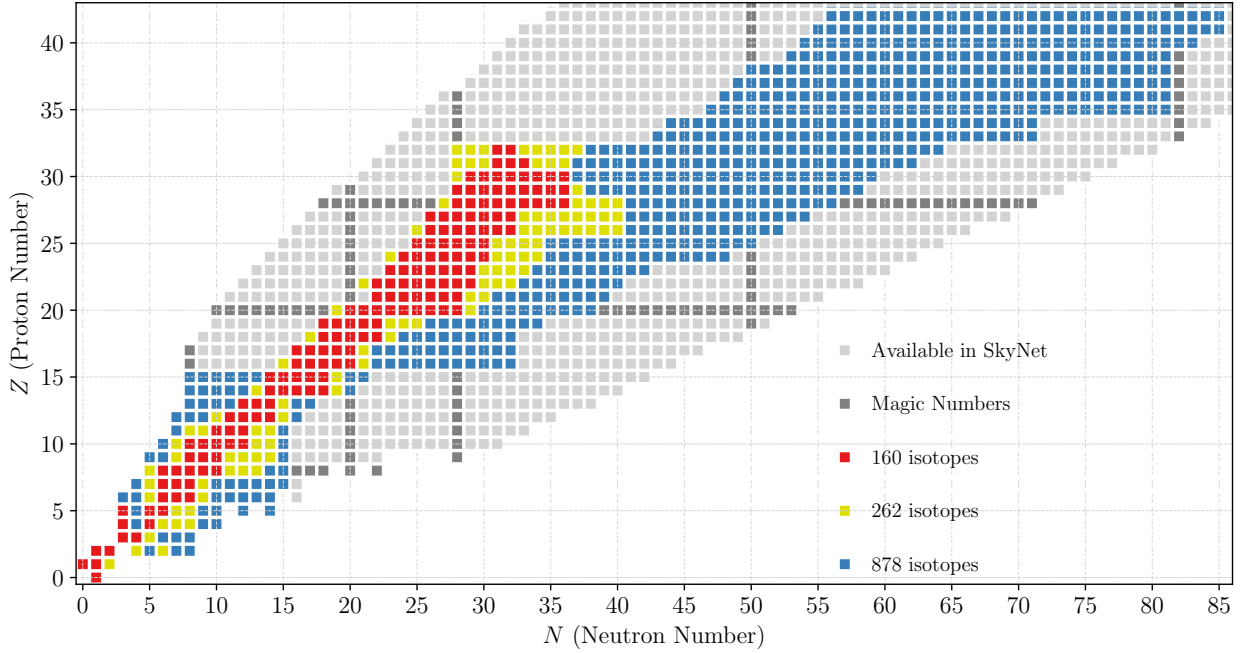


Figure 3. Nuclear chart visualizing the three sets of isotopes used in this work for testing the final nucleosynthetic outputs. The test calculations were done under extreme conditions of density, Y_e , and entropy, and were carried out until $t = 10$ s. Their results showed convergence in the final yields of the 50 most abundantly produced isotopes between the sets with 262 isotopes and 878 isotopes.

2.3 Reaction Networks

A small α -network is consistently coupled to the hydrodynamic modelling with P-HOTB. It is described in the relevant details by Müller (1986) and is capable of tracking the bulk nucleosynthesis and thus to account for the contribution to the explosion energy provided by explosive nuclear burning. The network includes the 13 isotopes of the alpha-chain, ^4He , ^{12}C , ^{16}O , ^{20}Ne , ^{24}Mg , ^{28}Si , ^{32}S , ^{36}Ar , ^{40}Ca , ^{44}Ti , ^{48}Cr , ^{52}Fe , and ^{56}Ni , plus a “tracer nucleus” ^{56}Tr , which is connected to the network with the reaction rates of ^{56}Ni and is supposed to keep track of the formation of neutron-rich species in matter with considerable neutron excess, i.e., when $Y_e < 0.49$ (Kifonidis et al. 2000, 2001, 2003). The network calculations made use of the reaction rates of Thielemann et al. (1996) and they were applied for temperatures between 0.1 GK and 9 GK, whereas for higher temperatures nuclear statistical equilibrium (NSE) was assumed.

In order to perform more detailed nucleosynthesis calculations of our models in a post-processing step, we made use of the modular nuclear reaction network library SkyNet (Lippuner & Roberts 2017). For this purpose we extracted the temperature and density evolution of selected mass-shell trajectories from our CCSN explosion simulations with P-HOTB and applied the SkyNet network to each of these shells, starting out with shells closest to the mass cut between ejecta and proto-neutron star and constraining the network calculations to the same regime in temperature as used for the small network in P-HOTB, namely to the interval between 0.1 GK and 9 GK. Adding up the nuclear abundances obtained for all mass shells that ended up to be ejected (i.e. that expanded outward continuously until the end of the hydrodynamic simulation) provided the integrated yields of chemical

elements and isotopes. If mass shells reached a peak temperature above $T_{\text{NSE}} = 9$ GK during their infall or explosive expansion, the network calculations were started only at the time when the temperature finally dropped below 9 GK, using the local NSE composition as initial condition.² Otherwise, if mass shells did not reach temperatures as high as 9 GK, the composition evolution of these mass shells was followed with SkyNet from the beginning of their infall through their shock heating and ejection, and the initial composition was taken from the progenitor data. The mass resolution for post-processing the nucleosynthesis was chosen to be $10^{-4} M_{\odot}$ for the innermost part of the ejecta below a stellar mass coordinate of $2 M_{\odot}$, and $0.005 M_{\odot}$ farther out.

SkyNet allows to define any selection of isotopes of interest and to define their relevant reactions. We took great care to employ a sufficiently big set of isotopes and to include all of their important reactions. To arrive there we started with three different sets of isotopes, inspired by their use in the literature: a small network with 160 isotopes (Sandoval et al. 2021), a medium-sized network with 204 isotopes (Paxton et al. 2015), and a large network with 822 isotopes (Woosley & Hoffman 1992). We modified the medium and the large ones in a way that every next-bigger list included the previous one. On top of that we added more light isotopes; for the largest network, for example, we included all nuclear species available in SkyNet with $Z \leq 15$ and $N \leq 15$. After these modifications, we ended up with selections of 160, 262, and 878 isotopes (see Figure 3). With all of these three versions of the network we performed nucleosynthesis calculations for about 20 trajectories with the most extreme conditions (in

² Note that any preceding nuclear composition is erased when NSE is established.

density, Y_e , and temperature) picked from the set of our CCSN models. We found that the yields were well determined with an accuracy of better than 1% for the 25 most abundantly produced isotopes when including 262 species compared to the case with 878 isotopes. Therefore we continued all further analyses with this medium-sized network, whose selection of nuclei is listed in Table 2.

In our present work, we will only discuss the production of ^{56}Ni based on our network calculations with the 262-isotope setup of SkyNet. We focus on this nickel isotope and aim at exploring the dependence of its production on the parameterisation of the thermal-bomb treatment, because the mass of ^{56}Ni ejected in the explosion is an important diagnostic quantity for CCSN observations (e.g., Arnett et al. 1989; Müller et al. 2017b; Yang et al. 2021; Valerin et al. 2022). Any implementation of a method to artificially trigger explosions in CCSN models should therefore be checked for its ability to provide reasonable predictions of the ^{56}Ni yield and for the robustness of these predictions concerning changes of the (mostly rather arbitrarily) chosen values of the parameters steering the trigger mechanism. The produced amount of ^{56}Ni is particularly useful to assess these questions, because the isotope is made in the innermost CCSN ejecta. Therefore it is potentially most immediately and most strongly affected by the artificial method (or by the physical mechanism) that is responsible for initiating the explosion.

3 THERMAL-BOMB SETUPS

In order to investigate the effects of the thermal-bomb parameterisation, we simulated models without a collapsing central core as well as models including the core collapse, varied the timescale t_{inj} of the energy deposition, changed the location of the inner grid boundary, and tested models with the volume ΔV for the energy deposition fixed in time instead of the mass layer ΔM being kept unchanged with time. Our naming convention for the CCSN models is the following:

- (i) U and C are used as first letters to discriminate between the uncollapsed and collapsed models.
- (ii) Numerical values refer to the ZAMS masses (in units of M_\odot) of the progenitor models. They are replaced by M_* as a placeholder in generic model names.
- (iii) Letters D or O are appended to distinguish the CCSN models with deep inner grid boundary at the progenitor’s location where $Y_e = 0.48$ from the models with the inner grid boundary farther out where $s/k_B = 4$.
- (iv) Letters M or M' at the end of the model names denote two different types of test simulations where the fixed mass value ΔM of the energy-injection layer is changed compared to the standard case with $\Delta M = 0.05 M_\odot$ (see Section 3.2).
- (v) Letters V instead of M at the end of the model names denote those simulations where the energy is injected into a fixed volume ΔV instead of a fixed mass shell ΔM .
- (vi) Letters xC at the beginning of the model names indicate that the collapse of these models was prescribed to reach an “extreme” radius, smaller than in the C-models.

A summary of all CCSN simulations studied for the four considered progenitor stars is given in Table 3. The explosion energy E_{exp} listed in this table is defined as the integral of the sum of the kinetic, internal, and gravitational energies

for all unbound mass, i.e., for all mass shells that possess positive values of the binding energy at the end of our simulation runs. We exploded our progenitors with an explosion energy of approximately $E_{\text{exp}} \approx 1\text{B} = 10^{51}\text{erg}$, guided by the values of 1.01 B for the $12.3 M_\odot$ and $19.7 M_\odot$ progenitors, 1.03 B for the $21.0 M_\odot$ star, and 1.07 B for the $26.6 M_\odot$ model.³ In all cases and setups, the energy was calibrated to the mentioned values with an accuracy of 3%, which is a good compromise between accuracy needed and effort required by the iterative process for the calibration to such a precision. The corresponding ranges of the explosion energies for each set of models with different energy-injection timescales are provided in the last column of Table 3. The slight differences in the explosion energies between the models of each set as well as between the different progenitors are of no relevance for the study reported here.

In detail, the different setups and corresponding simulations are as follows.

3.1 Models for comparison with SM19

We started our investigation with a setup that was guided by models discussed in SM19, i.e., the CCSN simulations did not include any collapse of the central core of the progenitors. These U-models were supposed to permit a comparison with the results presented by SM19.

In all of the discussed U-models the inner boundary was placed at the location where $Y_e = 0.48$, and in our default setup the explosion energy was injected into a fixed mass layer with $\Delta M = 0.05 M_\odot$, which was the same in all CCSN models for the set of progenitors. The inner boundary of this energy-deposition layer (IBED) was therefore chosen to be identical to the inner grid boundary. The entire mass exterior to the IBED, i.e., including the matter in the energy-deposition layer between the IBED and the outer boundary of the energy-deposition layer (OBED), was considered to be ejected, provided it became gravitationally unbound by the energy injection. Note that in models with fixed energy-deposition layer ΔM , the outer radius of this shell, R_{OBED} , moves outward as the heated mass ΔM expands, whereas the inner radius, R_{IBED} , is set to coincide with the inner grid boundary R_{IB} and does not change with time.

Our thus chosen setup differs in two technical aspects from the choices made in SM19. First, SM19 reported that they injected the thermal-bomb energy into a fixed mass of $0.005 M_\odot$ (corresponding to the innermost 20 zones of their 1D Lagrangian hydrodynamics simulations). In contrast, we adopted $\Delta M = 0.05 M_\odot$ as our default value. This larger mass appears more appropriate to us, at least in the case of the more realistic collapsed models and in view of the neutrino-driven mechanism, where neutrinos transfer energy to typically several $0.01 M_\odot$ to more than $0.1 M_\odot$ of circum-neutron star matter. Second, SM19 did not count the mass in the heated layer as ejecta, which means that they considered only the entire mass above the energy-deposition layer, i.e.,

³ These energies are slightly different in order to compare the thermal bomb models discussed here to existing neutrino-driven 1D explosion models from the study by Sukhbold et al. (2016) in a follow-up project.

Table 3. Properties of the thermal-bomb models computed in this work. M_{ZAMS} is the ZAMS mass of the progenitor star, “Model” is our name for the specific CCSN simulation (see text for our naming convention), “Inner Grid Boundary” specifies the criterion for placing the inner grid boundary, M_{ib} is the corresponding enclosed mass, t_{coll} is the collapse time, r_{min} is the minimum radius for the collapse phase, ΔM is the mass of the energy-injection layer or, respectively, the initial mass in the volume where the energy is injected, t_{inj} is the range of energy-deposition timescales considered, and E_{exp} is the range of final explosion energies to which the CCSN models for different energy-injection timescales were calibrated (see Section 3 for details). Note that per construction all $26.6 M_{\odot}$ models have identical values for ΔM in this listing (unless $\Delta M = 0.005 M_{\odot}$).

M_{ZAMS} [M_{\odot}]	Model	Inner Grid Boundary	M_{ib} [M_{\odot}]	t_{coll} [s]	r_{min} [cm]	ΔM [M_{\odot}]	t_{inj} [s]	E_{exp} [10^{51} erg]
12.3	U12.3D	$Y_e = 0.48$	1.230	no collapse	–	0.05	0.01 – 2.0	1.0099 – 1.0170
12.3	U12.3DM ¹	$Y_e = 0.48$	1.230	no collapse	–	0.005	0.01 – 2.0	0.9834 – 1.0241
19.7	U19.7D	$Y_e = 0.48$	1.256	no collapse	–	0.05	0.01 – 2.0	1.0003 – 1.0178
19.7	C19.7D	$Y_e = 0.48$	1.256	0.45	$5 \cdot 10^7$	0.05	0.01 – 2.0	1.0067 – 1.0125
19.7	C19.7O	$s/k_{\text{B}} = 4$	1.533	0.45	$5 \cdot 10^7$	0.05	0.01 – 2.0	1.0048 – 1.0160
19.7	xC19.7O	$s/k_{\text{B}} = 4$	1.533	0.45	$1.5 \cdot 10^7$	0.05	0.01 – 2.0	0.9977 – 1.0260
19.7	U19.7DM	$Y_e = 0.48$	1.256	no collapse	–	0.043	0.01 – 2.0	1.0018 – 1.0177
19.7	C19.7DM	$Y_e = 0.48$	1.256	0.45	$5 \cdot 10^7$	0.044	0.01 – 2.0	1.0016 – 1.0169
19.7	C19.7OM	$s/k_{\text{B}} = 4$	1.533	0.45	$5 \cdot 10^7$	0.027	0.01 – 2.0	1.0000 – 1.0151
19.7	U19.7DM ¹	$Y_e = 0.48$	1.256	no collapse	–	0.005	0.01 – 2.0	0.9889 – 1.0188
19.7	C19.7OM ¹	$s/k_{\text{B}} = 4$	1.533	0.45	$5 \cdot 10^7$	0.005	0.01 – 2.0	1.0061 – 1.0394
19.7	C19.7OV	$s/k_{\text{B}} = 4$	1.533	0.45	$5 \cdot 10^7$	0.027	0.01 – 0.5	0.9982 – 1.0302
19.7	xC19.7OV	$s/k_{\text{B}} = 4$	1.533	0.45	$1.5 \cdot 10^7$	0.027	0.01 – 2.0	1.0009 – 1.0400
21.0	U21.0D	$Y_e = 0.48$	1.272	no collapse	–	0.05	0.01 – 2.0	1.0185 – 1.0334
21.0	C21.0D	$Y_e = 0.48$	1.272	0.45	$5 \cdot 10^7$	0.05	0.01 – 2.0	1.0161 – 1.0302
21.0	C21.0O	$s/k_{\text{B}} = 4$	1.484	0.45	$5 \cdot 10^7$	0.05	0.01 – 2.0	1.0160 – 1.0266
21.0	xC21.0O	$s/k_{\text{B}} = 4$	1.484	0.45	$1.5 \cdot 10^7$	0.05	0.01 – 2.0	1.0210 – 1.0363
21.0	U21.0DM	$Y_e = 0.48$	1.272	no collapse	–	0.042	0.01 – 2.0	1.0207 – 1.0334
21.0	C21.0DM	$Y_e = 0.48$	1.272	0.45	$5 \cdot 10^7$	0.041	0.01 – 2.0	1.0205 – 1.0319
21.0	C21.0OM	$s/k_{\text{B}} = 4$	1.484	0.45	$5 \cdot 10^7$	0.068	0.01 – 2.0	1.0196 – 1.0247
21.0	U21.0DM ¹	$Y_e = 0.48$	1.272	no collapse	–	0.005	0.01 – 2.0	1.0251 – 1.0545
21.0	C21.0OM ¹	$s/k_{\text{B}} = 4$	1.484	0.45	$5 \cdot 10^7$	0.005	0.01 – 2.0	1.0067 – 1.0417
21.0	C21.0OV	$s/k_{\text{B}} = 4$	1.484	0.45	$5 \cdot 10^7$	0.068	0.01 – 1.0	1.0321 – 1.0503
21.0	xC21.0OV	$s/k_{\text{B}} = 4$	1.484	0.45	$1.5 \cdot 10^7$	0.068	0.01 – 2.0	1.0101 – 1.0346
26.6	U26.6D	$Y_e = 0.48$	1.383	no collapse	–	0.05	0.01 – 2.0	1.0677 – 1.0811
26.6	C26.6D	$Y_e = 0.48$	1.383	0.45	$5 \cdot 10^7$	0.05	0.01 – 2.0	1.0652 – 1.0784
26.6	C26.6O	$s/k_{\text{B}} = 4$	1.738	0.45	$5 \cdot 10^7$	0.05	0.01 – 2.0	1.0652 – 1.0775
26.6	xC26.6O	$s/k_{\text{B}} = 4$	1.738	0.45	$1.5 \cdot 10^7$	0.05	0.01 – 2.0	1.0595 – 1.0904
26.6	U26.6DM	$Y_e = 0.48$	1.383	no collapse	–	0.05	0.01 – 2.0	1.0677 – 1.0811
26.6	C26.6DM	$Y_e = 0.48$	1.383	0.45	$5 \cdot 10^7$	0.05	0.01 – 2.0	1.0652 – 1.0784
26.6	C26.6OM	$s/k_{\text{B}} = 4$	1.738	0.45	$5 \cdot 10^7$	0.05	0.01 – 2.0	1.0652 – 1.0775
26.6	U26.6DM ¹	$Y_e = 0.48$	1.383	no collapse	–	0.005	0.01 – 2.0	1.0492 – 1.0992
26.6	C26.6OM ¹	$s/k_{\text{B}} = 4$	1.738	0.45	$5 \cdot 10^7$	0.005	0.01 – 2.0	1.0562 – 1.1010
26.6	C26.6OV	$s/k_{\text{B}} = 4$	1.738	0.45	$5 \cdot 10^7$	0.05	0.01 – 1.0	1.0666 – 1.0855
26.6	xC26.6OV	$s/k_{\text{B}} = 4$	1.738	0.45	$1.5 \cdot 10^7$	0.05	0.01 – 2.0	1.0738 – 1.0985

Table 4. Parameters for our thermal-bomb models with fixed energy-deposition volume ΔV and models with variations of ΔM (except those with an extremely small value of $\Delta M = 0.005 M_{\odot}$). R_{IBED} and R_{OBED} are the inner and outer boundary radii of ΔV , ΔM is the initial mass in this volume, and the ratio gives the value of $R_{\text{OBED}}/R_{\text{IBED}}$. Since for each setup the $26.6 M_{\odot}$ model, uncollapsed or collapsed, was taken to calculate the radius ratio, $\Delta M = 0.05 M_{\odot}$ in all of the cases for this progenitor.

M_{ZAMS} [M_{\odot}]	UM*DM			CM*DM			CM*OM, CM*OV			xCM*OV		
	ΔM [M_{\odot}]	R_{IBED} [cm]	R_{OBED} [cm]	ΔM [M_{\odot}]	R_{IBED} [cm]	R_{OBED} [cm]	ΔM [M_{\odot}]	R_{IBED} [cm]	R_{OBED} [cm]	ΔM [M_{\odot}]	R_{IBED} [cm]	R_{OBED} [cm]
19.7	0.043	$1.066 \cdot 10^8$	$1.15 \cdot 10^8$	0.044	$5 \cdot 10^7$	$5.4 \cdot 10^7$	0.027	$5 \cdot 10^7$	$17.6 \cdot 10^7$	0.027	$1.5 \cdot 10^7$	$15.88 \cdot 10^7$
21.0	0.042	$1.058 \cdot 10^8$	$1.14 \cdot 10^8$	0.041	$5 \cdot 10^7$	$5.4 \cdot 10^7$	0.068	$5 \cdot 10^7$	$17.6 \cdot 10^7$	0.068	$1.5 \cdot 10^7$	$15.88 \cdot 10^7$
26.6	0.050	$1.278 \cdot 10^8$	$1.38 \cdot 10^8$	0.050	$5 \cdot 10^7$	$5.4 \cdot 10^7$	0.050	$5 \cdot 10^7$	$17.6 \cdot 10^7$	0.050	$1.5 \cdot 10^7$	$15.88 \cdot 10^7$
ratio		1.080			1.081			3.519			10.587	

exterior to the OBED, as ejecta. We did not join this convention, because we chose a 10 times larger mass for ΔM than SM19. In addition, again in view of the neutrino-driven mechanism, we do not see any reason why heated matter that can also be expelled should not be added to the nucleosynthesis-relevant CCSN ejecta. Moreover, we performed test calcula-

tions with $\Delta M = 0.005 M_{\odot}$ and found no significant differences in the ^{56}Ni yields, at least not in the case of uncollapsed models that served for a direct comparison with SM19. (This will be discussed in Section 4.4.)

The timescale of the energy deposition used in Equation (1)

was varied from 0.01 s to 2 s, using the following values:

$$t_{\text{inj}} = 0.01, 0.05, 0.2, 0.5, 1.0, 2.0 \text{ s}. \quad (3)$$

We thus tested the influence of different durations of the energy injection on the explosion dynamics and ^{56}Ni production. Although our progenitors are different from those used by SM19 and also our setup for the CCSN simulations differs in details from the one employed by SM19, the modelling approaches are sufficiently similar to permit us to reproduce the basic findings reported by SM19.

In Table 3 the corresponding models are denoted by UM_*D , where M_* stands here as a placeholder for the mass value of the model. While our standard setup uses $\Delta M = 0.05 M_\odot$, we also performed test runs with $\Delta M \approx 0.04 M_\odot$ for the U-setup. These models are denoted by UM_*DM in Table 3. We also ran test cases with the SM19 value of $\Delta M = 0.005 M_\odot$; the corresponding models are named UM_*DM' in Table 3, but they are not prominently discussed in the following, because such a small mass in the energy-deposition layer does not appear to be realistic for common CCSNe. It is most important, however, to note that all of these changes of ΔM led to secondary and never dominant differences in the produced amount of ^{56}Ni compared to the changes connected to introducing a collapse phase or shifting the inner grid boundary (see Section 3.2). We did not consider any cases UM_*O , because moving the inner grid boundary farther out will lead to lower densities in the ejecta (Figure 2). This will significantly reduce the nucleosynthesized amount of ^{56}Ni in this setup, and in particular for long t_{inj} it will lead to even more severe underproduction of ^{56}Ni compared to the yields inferred from observations of CCSNe with energies around 10^{51} erg (see Section 4.1).

3.2 Variations of thermal-bomb setups

Instead of releasing thermal energy in the uncollapsed progenitor as assumed by SM19, we extended our setup in a next step by forcing the progenitor's core to contract before depositing the energy. Adding such a collapse phase will change the dynamics of the explosion, even with the same explosion energy and the same location of the inner boundary.

To this end the inner grid boundary was moved inward for a time interval t_{coll} , thus mimicking the collapse phase that precedes the development of the explosion. The time-dependent velocity for contracting the inner boundary was prescribed as in Woosley & Weaver (1995); Woosley et al. (2002); Woosley & Heger (2007) (who applied this prescription within the framework of the classical piston method):

$$\frac{dr}{dt}(t) = v_0 - a_0 t \quad \text{for } t < t_{\text{coll}}, \quad (4)$$

where $v_0 < 0$ is the initial velocity of the inner boundary (following the infall of the progenitor model at the onset of its core collapse), and $a_0 = 2(r_0 - r_{\text{min}} + v_0 t_{\text{coll}})/t_{\text{coll}}^2$ is a constant acceleration calculated in order to reach the minimum radius r_{min} after the collapse time t_{coll} , with r_0 being the initial radius of the inner boundary. After this phase, the boundary contraction is stopped, matter begins to pile up around the grid boundary, and a shock wave forms at the interface to the still supersonically infalling overlying shells. Concomitantly, the deposition of internal energy by our thermal bomb was started.

Equation (4) defines the inward movement of the constant Lagrangian mass shell corresponding to the closed inner grid boundary. The collapse is basically controlled by the parameters t_{coll} and r_{min} , whereas the explosion phase is controlled by the thermal-bomb parameters E_{inj} , ΔM (or ΔV), and t_{inj} (Equations 1 and 2). Again following the literature mentioned above, we adopt for our default collapse simulations $t_{\text{coll}} = 0.45$ s and the minimum radius $r_{\text{min}} = 5 \cdot 10^7$ cm. In Table 3 the models with this collapse setup and the deep inner boundary are denoted by CM_*D . In these models the central (and maximum) densities lie between $7 \cdot 10^8 \text{ g cm}^{-3}$ and $2 \cdot 10^9 \text{ g cm}^{-3}$.

In a variation of the setup for the C-models, we relocated the inner grid boundary outward to the base of the oxygen shell in the progenitor, i.e., to the radial position where $s/k_B = 4$, with the goal of studying the influence on the ^{56}Ni production. These models are denoted by CM_*O in Table 3. The central (and maximum) densities of these models are between $3 \cdot 10^7 \text{ g cm}^{-3}$ and $2 \cdot 10^8 \text{ g cm}^{-3}$. A variant of these models, named xCM_*O , considered the collapse to proceed to a smaller radius of $r_{\text{min}} = 1.5 \cdot 10^7$ cm, using the same value of $t_{\text{coll}} = 0.45$ s for the collapse time. In this case the central (and maximum) densities reach the values between $3 \cdot 10^9 \text{ g cm}^{-3}$ and $9 \cdot 10^9 \text{ g cm}^{-3}$.

As in the U-models, the inner boundary of the grid and the inner boundary of the energy-deposition layer (IBED) were chosen to coincide in all simulations. In both model variants, U-models as well as C-models, our standard runs were done with energy being dumped into a fixed mass layer of mass $\Delta M = 0.05 M_\odot$. For the C-models we also simulated some test cases with different values of ΔM between about $0.03 M_\odot$ and roughly $0.07 M_\odot$. The corresponding models are denoted by CM_*DM or CM_*OM in Table 3. We also tested $\Delta M = 0.005 M_\odot$ in simulations with collapse and the IBED at $s/k_B = 4$, listed as models CM_*OM' in Table 3. These variations turned out to have no relevant influence on the ^{56}Ni yields in the D-boundary cases, in agreement with what we found for the U-models. However, the change of ΔM caused some interesting, though secondary, differences in those cases that employed the O-boundary. We will briefly discuss these results in Section 4.4.

In yet another variation we investigated cases for our more realistic setup of C-models with O-boundary, where the volume of the energy deposition, ΔV , was fixed instead of the mass layer ΔM . Such a change might potentially affect the ^{56}Ni production in CCSN models with steep density profile near the inner grid boundary. This time-independent volume of the energy deposition was determined for the different progenitors by a simple condition, connecting it to the initial values of the outer boundary radius R_{OBED} and of the inner boundary radius $R_{\text{IBED}} = R_{\text{ib}}$ of our standard setup with $\Delta M = 0.05 M_\odot$ in the $26.6 M_\odot$ CCSN models. Specifically, the volume ΔV , which is bounded by R_{IBED} and R_{OBED} , was defined by the requirement that the ratio of these two radii should have the same value as in the $26.6 M_\odot$ model in all of the CCSN runs (i.e., for all progenitors) of each considered setup:

$$\frac{R_{\text{OBED}}}{R_{\text{IBED}}}(26.6 M_\odot) = \frac{R_{\text{OBED}}}{R_{\text{IBED}}}(21.0 M_\odot) = \frac{R_{\text{OBED}}}{R_{\text{IBED}}}(19.7 M_\odot). \quad (5)$$

This condition means that the inner radius of the deposition

region, R_{IBED} , was pre-defined by R_{ib} in the O-cases, and the outer radii $R_{\text{OBED}}(21.0M_{\odot})$ and $R_{\text{OBED}}(19.7M_{\odot})$ were calculated from the equation above. The chosen condition of Equation (5) was also applied more generally for defining variations of ΔM (or ΔV) in collapsed or uncollapsed models with deep or outer location of R_{ib} (Table 4). Such a procedure should ensure that the distance between R_{IBED} and R_{OBED} adjusts to the size of R_{ib} and thus accounts for the higher density in its vicinity instead of being rigid without any reaction to the progenitors' radial structures.

The models with fixed energy-deposition volume ΔV thus determined are denoted by $CM_{*}\text{OV}$ or $xCM_{*}\text{OV}$ in Table 3 for standard and extreme collapse cases, respectively, and the values of R_{IBED} and R_{OBED} in our different model variations are listed in Table 4. The latter table also provides numbers for the initial masses ΔM that correspond to the volumes bounded by R_{IBED} and R_{OBED} . Note that Equation (5) implies that ΔM is still $0.05 M_{\odot}$ for the $26.6 M_{\odot}$ models, but the initial masses in the heating layers are not the same in the runs with fixed ΔV for the other progenitors. Of course, for fixed volume ΔV , the radii R_{IBED} and R_{OBED} do not evolve with time, but the mass ΔM in this heated radial shell decreases with time as the heated gas expands outward.

Table 4 also provides the ΔM values that were obtained via Equation (5) and apply for our tests performed with variations of the fixed heated mass-layer ΔM in models $UM_{*}\text{DM}$ (see Section 3.1) as well as models $CM_{*}\text{DM}$ and $CM_{*}\text{OM}$ mentioned above. These subsets of models are interesting despite their small differences in ΔM compared to our default choice of $\Delta M = 0.05 M_{\odot}$, because in the C-cases the initial volumes of the heated masses are the same for all progenitors instead of being different from case to case. Thus, these model variations check another aspect of potential influence on the nucleosynthesis conditions in the innermost ejecta.

4 RESULTS OF THERMAL-BOMB SIMULATIONS

In this section we present the results of our study, focusing on the mass of ^{56}Ni produced in the ejecta as computed in a post-processing step with the 262-isotope version of SkyNet (see Section 2.3). These yields were determined after 10 s of simulated evolution and, different from SM19, we usually (unless explicitly stated differently) considered as ejecta also unbound matter contained in the energy-deposition layer. We stress, however, that for models with the deep inner boundary $R_{\text{ib}} = R_{\text{IBED}}$ at $Y_e = 0.48$, there is no relevant difference in the ^{56}Ni yields when including or excluding the mass in the heating layer. The reason is seen in Figure 2, upper and lower right panels: Since $Y_e < 0.485$ in the innermost $0.05 M_{\odot}$ just outside of R_{ib} , i.e., in the mass between R_{IBED} and R_{OBED} , the ^{56}Ni production is negligibly small in the energy-deposition layer.

In Section 4.1 we will first report on our models of the U-setup in comparison to SM19. Then, in Section 4.2, we will discuss the differences when our models included an initial collapse before the thermal bomb was switched on. In Section 4.3 we will describe the influence of shifting the inner grid boundary, $R_{\text{ib}} = R_{\text{IBED}}$, from the deep default location at $Y_e = 0.48$ to the outer location at the base of the oxygen shell where $s/k_B = 4$. In Section 4.4 we will briefly summa-

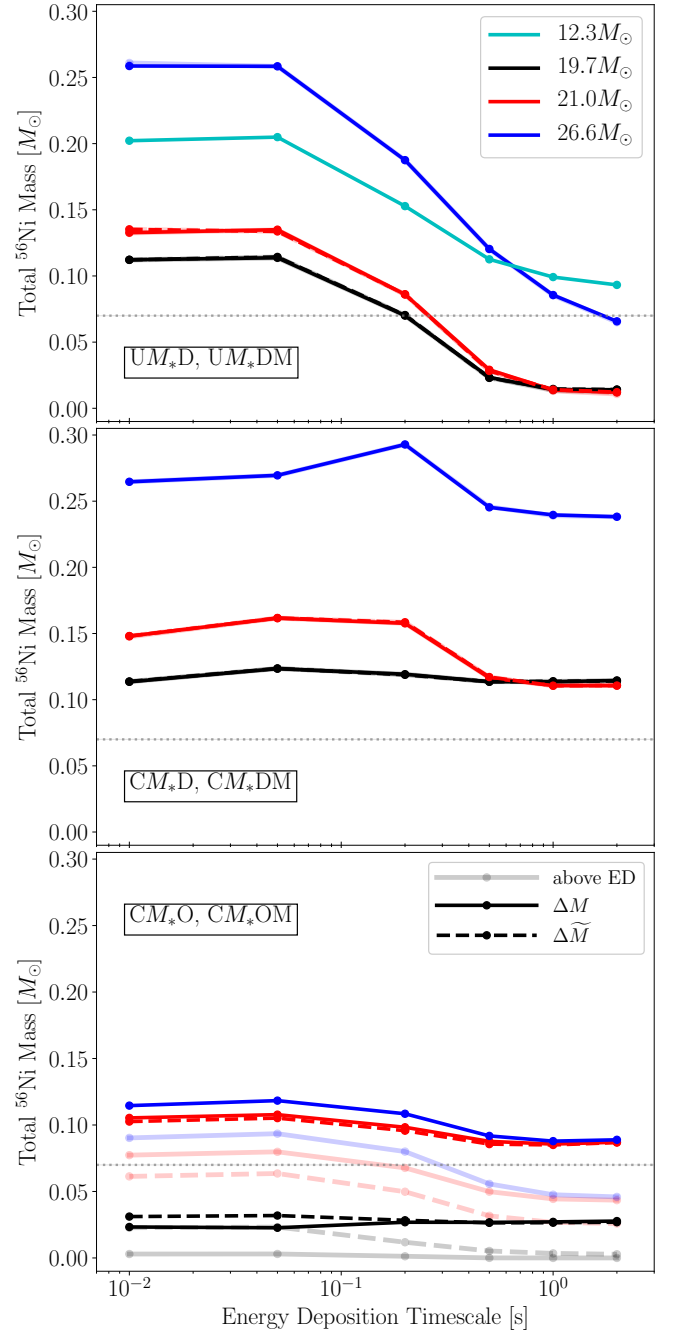


Figure 4. ^{56}Ni yields as functions of energy-injection timescale for uncollapsed CCSN models (top panel) and collapsed models (middle panel) with deep inner grid boundary, and collapsed CCSN models with the inner grid boundary shifted farther out (bottom panel). The different colors correspond to the different progenitors as labelled in the top panel. Solid lines belong to our standard choice of $\Delta M = 0.05 M_{\odot}$ for the fixed mass in the energy-deposition layer and dashed lines refer to varied mass values $\Delta \tilde{M}$ (models with unprimed M in their names; see Table 3). Note that in the top and middle panels the solid and dashed lines overlap and are almost completely indistinguishable. In all panels the blue solid and dashed lines fall on top of each other by definition. The light-colored lines (solid and dashed) in the bottom panel show the ^{56}Ni yields when the mass in the energy-injection layer is excluded from the ejecta instead of adding unbound matter of this layer to the ejecta. The horizontal grey dotted line indicates the ^{56}Ni yield of $0.07 M_{\odot}$ for a $\sim 10^{51}$ erg explosion, e.g., SN 1987A (Arnett et al. 1989).

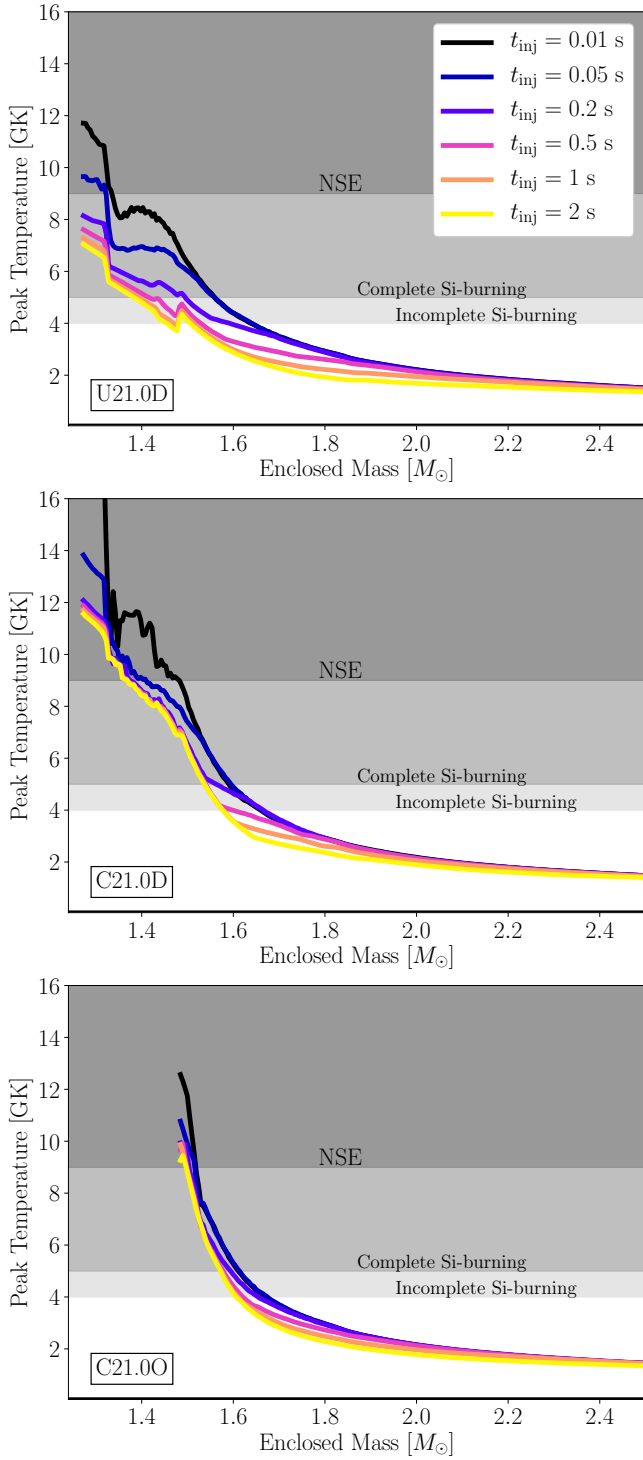


Figure 5. Peak temperatures as functions of enclosed mass for the CCSN runs with the $21 M_{\odot}$ progenitor and different energy-injection timescales for the same modelling setups shown in Figure 4: uncollapsed (top), collapsed (middle), and collapsed with inner grid boundary shifted farther out (bottom). Different intensities of grey shading indicate different regimes of explosive nucleosynthesis as labelled. Note that the peak temperatures are displayed only for the runs with our standard value of $\Delta M = 0.05 M_{\odot}$ for the fixed mass in the energy-injection layer, because the differences compared to the other choices of ΔM are effectively indistinguishable.

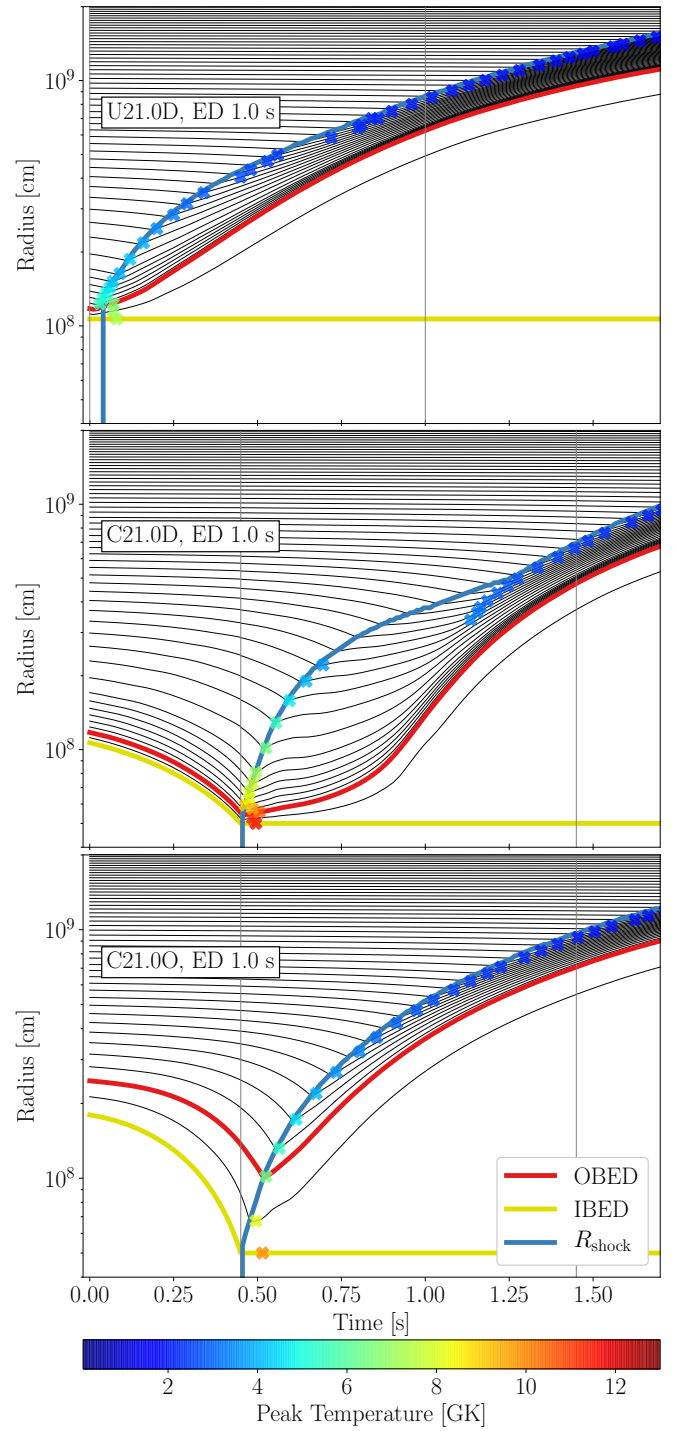


Figure 6. Radius evolution of Lagrangian mass shells with time for the CCSN runs of the $21 M_{\odot}$ progenitor with standard value of $\Delta M = 0.05 M_{\odot}$ for the fixed mass in the energy-injection layer and a representative energy-deposition timescale of 1.0 s: uncollapsed (top) and collapsed (middle) with deep inner grid boundary, and collapsed with inner grid boundary shifted farther out (bottom). The thin black solid lines are the mass shells, spaced in steps of $0.025 M_{\odot}$, the blue line marks the shock radius, the red line indicates the radius of the outer edge of the energy-injection layer (R_{OBED}), and the yellow line the radius of the inner grid boundary, R_{IB} , which is chosen as the inner edge of the energy-injection layer (R_{IBED}) when the thermal bomb is switched on. Crosses indicate the moments when the peak temperature of each mass shell is reached; their colors correspond to temperature values as given by the color bar. Vertical lines mark the beginning and the end of the energy deposition.

rize the consequences of changing the fixed mass ΔM of the energy-deposition layer, in Section 4.5 we will discuss the influence of changing from a fixed mass ΔM to a fixed volume ΔV of the energy-injection layer, and in Section 4.6 we will finally present results for different minimum radii prescribed for the collapse phase.

4.1 Uncollapsed models compared to SM19

When we consider uncollapsed models with deep inner grid boundary and the thermal-bomb energy injection into a fixed mass ΔM (the UM_*D simulations), following SM19, our results confirm the findings of this previous study (Figure 4, top panel): One can witness a clear anti-correlation between the amount of ^{56}Ni produced and the timescale of the energy deposition for the explosion runs of all of the four considered progenitors; slower energy injection leads to a clear trend of reduced ^{56}Ni production.

Our set of CCSN models exhibits the same qualitative behavior as visible in Figure 7 (left panel) of SM19, although there are significant quantitative differences. These are most likely connected to the different core structures of the progenitor models, because the mentioned technical differences in the explosion modelling (i.e., the choice of the value of ΔM for the energy-injection layer and the inclusion of the heated mass in the ejecta) turned out to have no significant impact on the ^{56}Ni yields in the uncollapsed models with deep inner boundary, see Sections 4.3 and 4.4. For example, we investigated the effects of changing ΔM within several 10% of our standard value (varying between $0.027 M_\odot$ and $0.068 M_\odot$) and also tested the extremely small value of $\Delta M = 0.005 M_\odot$, but could not find any relevant ^{56}Ni differences compared to our UM_*D simulations (a detailed discussion of this aspect is provided in Section 4.4).

The reason for the anti-correlation of ^{56}Ni yield and energy-injection timescale can be inferred from the top panel of Figure 5, which displays the peak temperatures as functions of enclosed mass for all investigated values of t_{inj} in the $21 M_\odot$ CCSN runs. Efficient ^{56}Ni production requires the temperature in the expanding ejecta to reach the regime of NSE or complete silicon burning. Moreover, Y_e has to exceed ~ 0.48 considerably, which is obvious from the upper and lower right panels of Figure 2, where ^{56}Ni mass fractions above 0.1 occur only in regions where $Y_e \gtrsim 0.485$. Only when these requirements are simultaneously fulfilled, freeze-out from NSE or explosive nuclear burning are capable of contributing major fractions to the ^{56}Ni yield. The top panel of Figure 5 shows that for longer energy-injection times not only the maximum value of the peak temperature that can be reached in the heated matter drops, but also the total mass that is heated to the threshold temperature of complete Si burning (about 5 GK) decreases. Therefore less ^{56}Ni is nucleosynthesized when the energy injection of the thermal bomb (for a given value of the final explosion energy) is stretched over a longer time interval.

This behavior is a consequence of the fact that the heated matter begins to expand as soon as the thermal bomb is switched on (see the upper panel of Figure 6 for the uncollapsed $21.0 M_\odot$ model with $t_{\text{inj}} = 1.0\text{ s}$). When the energy injection is quasi-instantaneous, i.e., short compared to the

hydrodynamical timescale for the expansion,⁴ the thermal energy deposition leads to an abrupt and strong increase of the temperature before the matter can react by its expansion. If, in contrast, the energy release by the thermal bomb for the same final explosion energy is spread over a long time interval, i.e., longer than the hydrodynamical timescale, the expansion occurring during this energy injection has two effects that reduce the temperature increase, in its maximum peak value as well as in the volume that gets heated to high temperatures: First, cooling by expansion (pdV) work limits the temperature rise and, second, the thermal energy dumped by the bomb is distributed over a wider volume because the fixed mass ΔM , into which the energy is injected, expands continuously. This is visible in the mass-shell plots of Figure 6 by the outward motion of the red line, which corresponds to the outer boundary radius, R_{OBED} , of the energy-deposition layer. Because the gravitational binding energy of the uncollapsed stellar profile is comparatively low, the expansion of the energy-injection layer sets in basically promptly when the thermal bomb starts releasing its energy at $t = 0$. This holds true even if the specific energy-deposition rate $\dot{e}_{\text{inj},M}$ is relatively low because of a long injection timescale of $t_{\text{inj}} = 1.0\text{ s}$, for example (top panel of Figure 6).

Comparing the results for the four progenitors in the top panel of Figure 4, we notice three different aspects: (i) The absolute amount of the produced ^{56}Ni and its steep variation with t_{inj} are quite similar for the $19.7 M_\odot$ and $21 M_\odot$ progenitors; (ii) these progenitors yield considerably less ^{56}Ni for all energy-injection timescales than the $26.6 M_\odot$ case; (iii) the $12.3 M_\odot$ progenitor exhibits the weakest variation of the ejected ^{56}Ni mass with t_{inj} among all of the four considered stars.

These differences can be traced back to the progenitor structures plotted in Figure 2 and to the peak temperature profiles in the ejecta caused by the thermal bomb (see top panel in Figure 7). Because of the shallow density profile at $r > R_{\text{ib}}$ in the $26.6 M_\odot$ progenitor, the outward going shock wave that is generated by a thermal bomb with final explosion energy of 10^{51} erg heats much more mass to the temperatures required for strong ^{56}Ni production. The ^{56}Ni nucleosynthesis is actually hampered in the $26.6 M_\odot$ progenitor by the fact that its innermost layer of $\sim 0.15 M_\odot$ possesses Y_e values below 0.485 (Figure 2, upper right panel). In such conditions the mass fraction of ^{56}Ni does not exceed a few percent, see Figure 2, lower right panel, and Figure 8, top panel, for $t_{\text{inj}} = 0.01\text{ s}$ and $t_{\text{inj}} = 1.0\text{ s}$, respectively. Nevertheless, the $26.6 M_\odot$ runs produce a lot of ^{56}Ni because considerable abundances of this isotope can be nucleosynthesized even beyond an enclosed mass of $\sim 1.8 M_\odot$, in particular for short energy-injection times.

In contrast, the $12.3 M_\odot$ progenitor possesses only a narrow layer of less than $\sim 0.07 M_\odot$ with $Y_e \lesssim 0.485$ around R_{ib} . This enables a relatively abundant production of ^{56}Ni in the

⁴ The hydrodynamical timescale, by its order of magnitude, is given by the radial extension of the bomb-heated layer divided by the average sound speed in this layer. For the uncollapsed models it is roughly $\Delta R/c_s \sim 10^7 \text{ cm}/(10^9 \text{ cm s}^{-1}) = 10^{-2} \text{ s}$. Since the gravitational binding energy of the uncollapsed stellar structure at $r > R_{\text{ib}}$ is low, this means that the outward expansion of the thermal-bomb-heated layer gains momentum within several 10 ms at the longest.

thermal-bomb models with this star for all energy-injection times and in spite of the steeper density profile compared to the $26.6 M_{\odot}$ progenitor. Finally, the two stellar models with $19.7 M_{\odot}$ and $21 M_{\odot}$ exhibit very similar Y_e profiles and also their density profiles are close to each other up to the base of the oxygen shell, which is at roughly $1.48 M_{\odot}$ in the $21 M_{\odot}$ model, but at about $1.53 M_{\odot}$ in the $19.7 M_{\odot}$ case (see Table 1). This difference, however, is located quite far away from the inner grid boundaries (which are at $1.256 M_{\odot}$ and $1.272 M_{\odot}$ for $19.7 M_{\odot}$ and $21 M_{\odot}$, respectively; see Table 3) and its consequence (i.e., higher ^{56}Ni mass fractions up to larger mass coordinates in the $21.0 M_{\odot}$ runs; Figure 8) is partly compensated by more efficient ^{56}Ni production in the layers just exterior to the energy-injection domain in the $19.7 M_{\odot}$ runs (Figure 2, lower right panel, and Figure 8, top panel). The overall effect is that both progenitors resemble each other closely in their ^{56}Ni outputs for all values of t_{inj} , at least when uncollapsed thermal-bomb models with deep inner boundary are considered.

In the following we will not use the $12.3 M_{\odot}$ runs any further, because they exhibit the weakest variation of the produced ^{56}Ni mass with t_{inj} , whereas our main focus is on how this variation is affected when an initial collapse phase is included in the thermal-bomb treatment.

4.2 Collapsed models

The picture changes radically when a collapse phase is introduced into the explosion modelling before the energy injection by the thermal bomb is switched on Figure 4, middle panel, displays the ^{56}Ni yields for the corresponding models with deep inner boundary (our $CM_{*}D$ simulations). For short energy-injection timescales ($t_{\text{inj}} \lesssim 0.05$ s) we find amounts of ^{56}Ni very similar to those obtained in the uncollapsed models, but now also the explosion simulations with longer t_{inj} are efficient in producing ^{56}Ni . In fact, there is little variation of the ^{56}Ni yields when t_{inj} increases from 0.01 s to 2 s. The anti-correlation of the ^{56}Ni production with t_{inj} observed for the $UM_{*}D$ models is gone and instead the $CM_{*}D$ models exhibit a ^{56}Ni nucleosynthesis that varies much less with the duration of the energy release by the thermal bomb.

Inspecting the peak temperature profiles versus enclosed mass (Figure 5, middle panel), one recognizes three main differences compared to the uncollapsed cases in the top panel of this figure. First, the maximum peak temperatures for all energy-injection times reach higher values in the C-models and extend well into the NSE regime. Second, the peak temperature profiles are more similar to each other than in the U-models when t_{inj} is varied. And third, this implies that for all values of t_{inj} a wider mass layer is heated to the temperatures required for complete Si burning or NSE.

These differences in the collapsed models compared to the uncollapsed ones have several reasons, whose relative importance varies with the energy-injection timescale. Because of the compression heating during the collapse, the temperatures at the onset of the energy injection by the thermal bomb are already higher. A more important effect, however, is connected to the fact that the shock expands into stellar layers that have collapsed for ~ 0.5 s or longer and over radial distances between several 100 km and more than 1000 km. The growing kinetic energy of the infalling gas is converted to thermal energy in the shock. Moreover, the energy in-

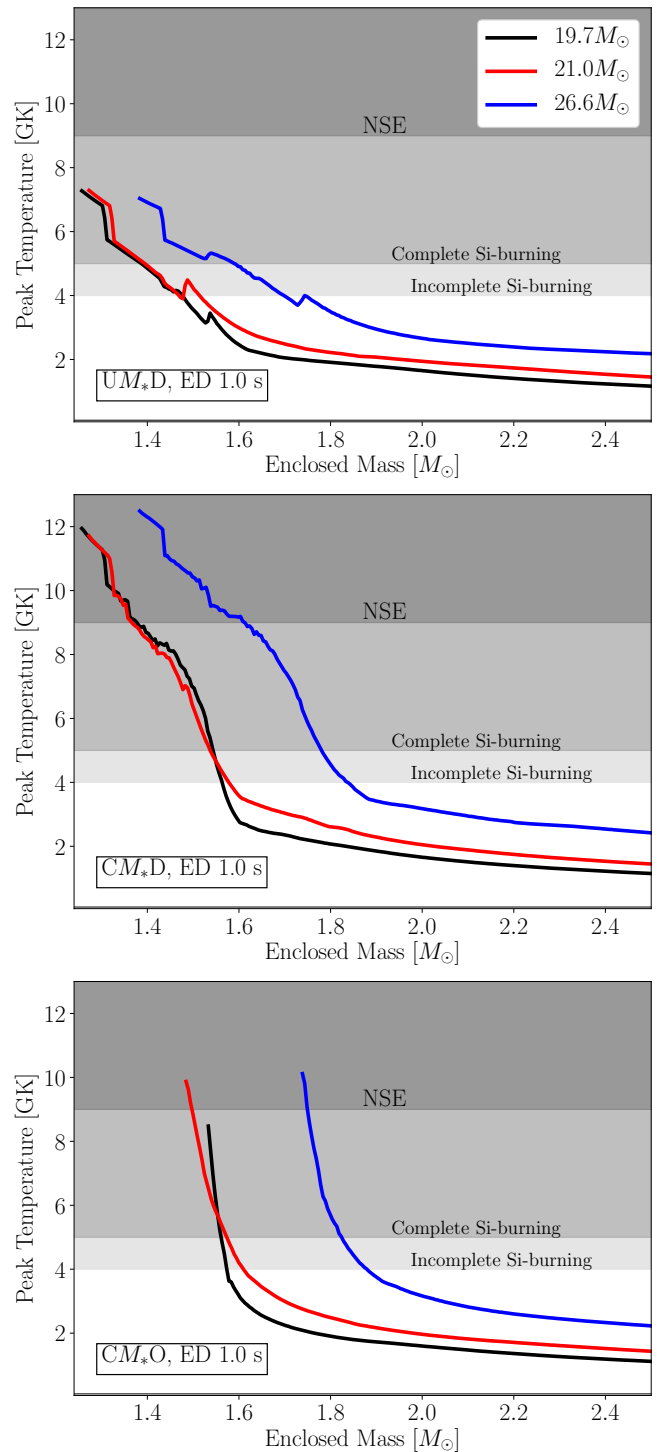


Figure 7. Peak temperatures as functions of enclosed mass for CCSN models for different progenitors using the standard value of $\Delta M = 0.05 M_{\odot}$ for the fixed mass in the energy-injection layer and a representative energy-deposition timescale of 1.0 s: uncollapsed (top) and collapsed (middle) with deep inner grid boundary, and collapsed with inner grid boundary shifted further out (bottom). Grey shading again indicates different regimes of explosive nucleosynthesis as in Figure 5. Note that the peak temperatures are displayed only for the runs with our default choice of $\Delta M = 0.05 M_{\odot}$, because the differences compared to the other choices of ΔM are effectively indistinguishable.

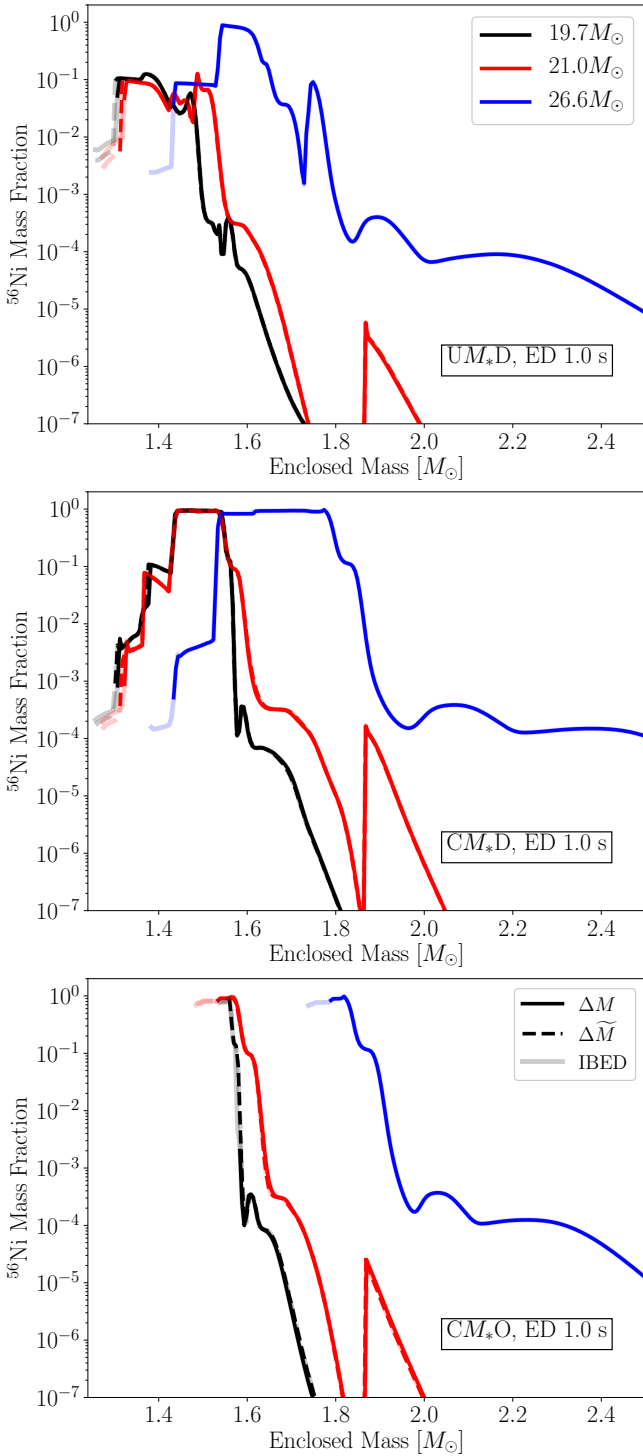


Figure 8. ^{56}Ni mass fractions as functions of enclosed mass as produced in the CCSN models shown in Figure 7. Here, we plot the results for our standard value of $\Delta M = 0.05 M_{\odot}$ for the fixed mass in the energy-injection layer (solid lines) and for the cases with varied mass values $\widetilde{\Delta M}$ (models with unprimed M in their names, see Table 3; dashed lines). Note that the solid and dashed lines mostly overlap and therefore are hardly distinguishable. Moreover, we highlight the contribution to the ^{56}Ni production from the mass in the energy-injection layer, which is included in our definition of the ejecta (indicated by light-colored parts of the solid and dashed lines).

put into the collapsed mass layer of $\Delta M = 0.05 M_{\odot}$ means that the energy is injected into a much smaller volume than in the uncollapsed models (Table 4), implying considerably higher heating rates per unit volume. For the uncollapsed $26.6 M_{\odot}$ model with deep inner boundary, for example, the initial radii bounding the heating layer are $R_{\text{IBED}} \approx 1280$ km and $R_{\text{OBED}} \approx 1380$ km, i.e., the layer has a width of ~ 100 km, whereas in the corresponding collapsed model the initial radial extension of the heating layer is only 40 km between 500 km and 540 km (see Table 4). In addition, the expansion of the heated matter sets in much more slowly in the collapsed models, where the energy-injection layer sits deeper in the gravitational potential and the overlying, infalling mass shells provide external pressure, hampering the outward acceleration. One can clearly see this effect when comparing the top and middle panels of Figure 6. This inertia of the matter in the wake of the outgoing shock permits the energy injection to boost the temperature and thus the postshock pressure to high values even when the energy-deposition timescales are long. As a consequence, the shock is pushed strongly into the infalling, overlying shells, and the peak-temperature profiles (Figure 5) as well as the mass that is heated sufficiently to enable abundant ^{56}Ni production become quite similar for different t_{inj} .

Again, as for the U-models, the thermal-bomb runs for the collapsed $26.6 M_{\odot}$ models lead to the highest yields when the final explosion energy is fixed to $\sim 10^{51}$ erg for all progenitors. Once again, this is connected to the more shallow pre-collapse density profile of the $26.6 M_{\odot}$ star, for which reason more mass is heated to ^{56}Ni -production temperatures (Figure 7, middle panel). Correspondingly, the mass layer with a high mass fraction of this isotope is much more extended in the C26.6 models (see Figure 8, middle panel). More energy input by the thermal bomb is needed and, accordingly, a stronger shock wave is created to lift the ejecta out of the deeper gravitational potential of the central mass of the new-born neutron star ($M_{\text{ib}} = 1.383 M_{\odot}$ in model C26.6D compared to $1.256 M_{\odot}$ and $1.272 M_{\odot}$ in models C19.7D and C21.0D, respectively).

The ^{56}Ni yields of the $19.7 M_{\odot}$ and $21.0 M_{\odot}$ models are somewhat more different in the simulations with initial collapse than in the runs without collapse, especially for energy-injection times shorter than 0.5 s (Figure 4, middle panel), despite the similar density profiles of the two stars up to the base of the oxygen shell and despite their steep increase from $Y_e < 0.485$ to $Y_e > 0.495$ happening at the same mass coordinate (Figure 2, upper two panels). The C21.0D models nevertheless produce more ^{56}Ni because the interface to the O-layer with decreasing density and increasing entropy lies at a lower enclosed mass, permitting stronger shock heating and more ^{56}Ni nucleosynthesis in the oxygen shell (Figure 8, middle panel). For long energy-injection times, however, this effect is again compensated by slightly more ^{56}Ni production in the innermost layers of the C19.7D runs.

A special feature requires brief discussion: At intermediate energy-deposition timescales the C21.0D and C26.6D models exhibit local maxima of their ^{56}Ni yields, more prominently in the $26.6 M_{\odot}$ cases and only shallow in the $21.0 M_{\odot}$ runs. This phenomenon is caused by the thermal-bomb prescription of energy-injection into a fixed mass shell ΔM that starts expanding when the energy deposition takes place on

a shorter timescale than the expansion, which leads to peak temperatures in the ejecta that are reached not exactly right behind the outgoing shock wave but at some distance behind the shock, thus causing high temperatures for a longer period in a wider layer of mass and therefore more ^{56}Ni production. This effect can be seen in a weak variant in the middle panel of Figure 6, where between $t \sim 1.1$ s and $t \sim 1.3$ s the peak temperatures of the expelled mass shells (marked by crosses) appear detached from the shock. In this $21.0 M_{\odot}$ model with $t_{\text{inj}} = 1.0$ s, however, the effect is mild and has no relevant impact on the ^{56}Ni nucleosynthesis. For simulations with very short t_{inj} the energy deposition is so fast that the compression wave quickly merges with the shock, whereas for very long timescales t_{inj} the energy injection is gentle and keeps pace with the outward acceleration of the mass shells, for which reason a strong compression wave is absent. Only at intermediate values of $t_{\text{inj}} \sim 0.2$ s this compression wave has a significant influence on the temperature evolution of the ejected mass shells in the postshock domain and thus a noticeable effect on enhanced ^{56}Ni production.

4.3 Shifted inner boundary

In a next test we moved the inner grid boundary from the deep location to the position at the base of the O-shell (where $s/k_{\text{B}} = 4$). This choice for the $CM_{*}O$ models is more realistic than the deep inner boundary, because it is better compatible with our current understanding of the neutrino-driven explosion mechanism of CCSNe (e.g., Ertl et al. 2016; Sukhbold et al. 2016). The corresponding ^{56}Ni yields of the thermal-bomb simulations with our standard setting of $\Delta M = 0.05 M_{\odot}$ for the energy-injection layer and different values of t_{inj} are displayed by solid lines in the bottom panel of Figure 4.

First, we notice that the ^{56}Ni yields of $CM_{*}O$ models are much lower for all t_{inj} than in the $CM_{*}D$ models in the panel above. In absolute numbers these yields are closer to the typical values of $\sim 0.05\text{--}0.1 M_{\odot}$ for the ^{56}Ni production in CCSNe with explosion energies around $(1\text{--}2) \times 10^{51}$ erg (see, e.g., Arnett et al. 1989; Iwamoto et al. 1994; Müller et al. 2017b). While models C26.6O and C21.0O eject similar amounts of ^{56}Ni , model C19.7O, in contrast, produces considerably less ^{56}Ni .

Several important aspects in the C-models with the O-boundary are different from those with the D-boundary: The densities and therefore the ram pressure in the pre-shock matter are significantly lower, for which reason the expansion of the shock and thus also of the matter in the energy-injection layer and above occurs much faster. This can be seen by comparing the middle and bottom panels of Figure 6. Moreover, since the density is low, the energy injected into a given mass layer ΔM is distributed over a considerably wider volume, which can be concluded from the values of R_{OBED} given for the $CM_{*}O$ and $CM_{*}D$ models in Table 4 ($1.76 \cdot 10^8$ cm and $5.4 \cdot 10^7$ cm, respectively). The effect, however, is not quite as dramatic as the different R_{OBED} might suggest, because the density gradient is steep and most of the heated mass ΔM is still located relatively close to $R_{\text{IBED}} = 5 \cdot 10^7$ cm. Overall, however, these differences lead to steeper declines of the peak temperatures with enclosed mass than in the models with D-boundary (compare the bottom panels of Figures 5 and 7 with the top and middle panels of these figures). This

explains why in the CCSN models with O-boundary less mass is heated to ^{56}Ni production temperatures. As a consequence, the layer of abundant ^{56}Ni nucleosynthesis is much narrower in mass and very close to the inner grid boundary (Figure 8), and the total ^{56}Ni yields are considerably lower than in the CCSN models with deep boundary, even when the final explosion energy is tuned to the same value.

In the $CM_{*}O$ models the peak temperature profiles are quite similar for different energy-injection timescales (Figure 5, bottom panel), for which reason the ^{56}Ni outputs of the $21.0 M_{\odot}$ and $26.6 M_{\odot}$ models are relatively similar with a moderate decrease for longer t_{inj} . In the case of the $19.7 M_{\odot}$ simulations, however, the peak temperature declines extremely steeply as function of enclosed mass (Figure 7) because of the very low densities of the heated mass layer (due to the low densities in the oxygen layer of the progenitor; Figure 2). Therefore the expansion of this layer proceeds extremely quickly and the expansion cooling as well as the dilution of the energy deposition over a quickly growing volume do not permit high peak temperatures in a large mass interval. This leads to the result that the ^{56}Ni yields in the C19.7O models are the lowest of all of the three considered progenitors.

Another difference between C-models with D-boundary and O-boundary is the fact that in the latter the inclusion of the heated mass ΔM in the ejecta or its exclusion can make a sizable difference in the ^{56}Ni yields. In contrast to the $UM_{*}D$ and $CM_{*}D$ models, the simulations with collapse and O-boundary produce considerably less ^{56}Ni when the matter in the energy-injection layer is not taken into account in the ejecta (see the light-colored solid lines in the bottom panel of Figure 4). In particular, C19.7O underproduces ^{56}Ni massively in this case, and for the models with the $21.0 M_{\odot}$ and $26.6 M_{\odot}$ progenitors we witness again a strong trend of decreasing ^{56}Ni yields with longer energy-injection timescales when only material exterior to R_{OBED} is counted as ejecta.

Such a trend, however, disappears essentially entirely when the ^{56}Ni nucleosynthesized in the energy-deposition layer is included in the ejecta (heavy solid lines compared to light-colored solid lines in the bottom panel of Figure 4). We recall that the exclusion of the heated mass from the ejecta or its inclusion does not have any relevant influence on the total ^{56}Ni yields of our U- and C-models with deep inner boundary, because the low Y_e in the vicinity of this boundary location (see Figure 2) prevents abundant production of ^{56}Ni in the heated mass layer (Figure 8, top and middle panels). The situation is different now for the O-models, because Y_e is close to 0.5 near the inner grid boundary in this case (Figure 2). Much of the ^{56}Ni is then produced in the mass layers just exterior to R_{ib} in addition to the fact that the total ^{56}Ni yields are much smaller (Figure 8, bottom panel). Therefore the ^{56}Ni assembled in the heated mass can make a significant or even dominant contribution to the total yield of this isotope. The C19.7O models are the most extreme cases in this respect. Their ^{56}Ni yields are extremely low when only matter exterior to the heated layer is considered as ejecta. This is especially problematic since our default value of $0.05 M_{\odot}$ for the energy-injection mass ΔM is fairly large. This fact is further illuminated in the following section, where we will discuss the results for variations of ΔM .

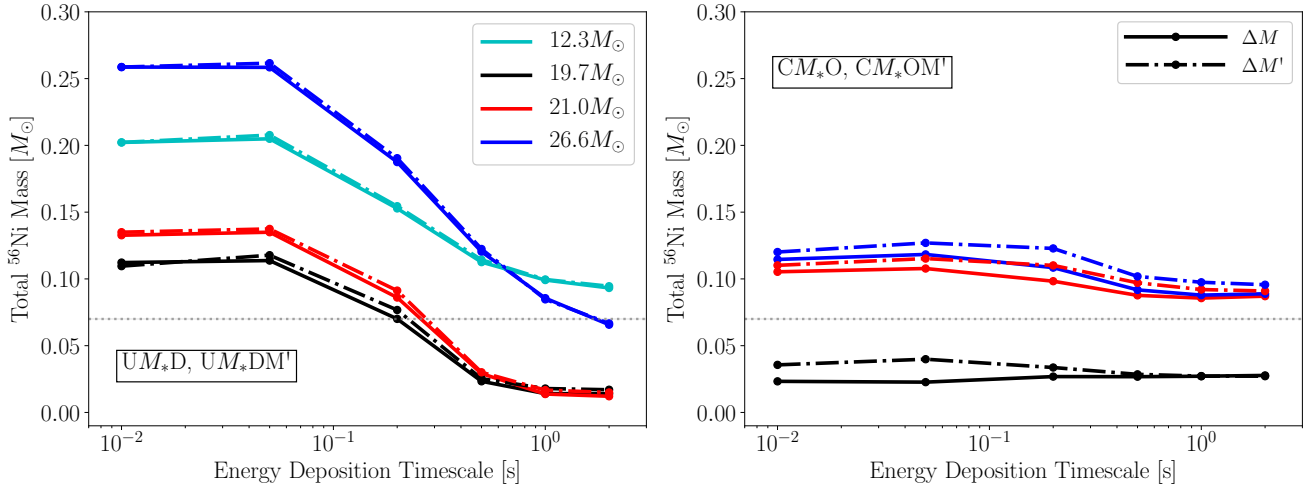


Figure 9. ^{56}Ni yields as functions of energy-injection timescale for uncollapsed CCSN models (left panel) and collapsed CCSN models with inner grid boundary shifted farther out (right panel). The different colors correspond to the different progenitors as labelled in the left panel. Solid lines belong to our standard choice of $\Delta M = 0.05 M_{\odot}$ for the fixed mass in the energy-deposition layer and dash-dotted lines refer to the values of $\Delta M' = 0.005 M_{\odot}$ (see Table 3). The horizontal grey dotted line indicates the ^{56}Ni yield of $0.07 M_{\odot}$ for a $\sim 10^{51}$ erg explosion, e.g., SN 1987A (Arnett et al. 1989).

4.4 Variations of mass in energy-injection layer

We also simulated some test cases of U-models and C-models using moderately different values of the fixed heated mass ΔM , varied within plausible ranges such that the initial volumes of the heated masses are the same for the C-models of all progenitors (see Table 4 and Section 3.2). These models are denoted by $UM_{*}DM$, $CM_{*}DM$, and $CM_{*}OM$, represented by dashed lines in the panels of Figure 4.

There are no relevant effects with respect to the ^{56}Ni production, neither in U-models nor C-models, in the cases with deep inner boundary when $\Delta M \approx 0.04 M_{\odot}$ is used instead of $\Delta M = 0.05 M_{\odot}$; the dashed lines are mostly indistinguishable from the solid lines in the top and middle panels of Figure 4. However, slightly more sensitivity of the ^{56}Ni yields to the choice of ΔM is obtained in the cases of the $CM_{*}O$ models (bottom panel of Figure 4). Changing to $\Delta M \approx 0.03 M_{\odot}$ (C19.7OM models) increases the nickel production for $t_{\text{inj}} \lesssim 0.2$ s, whereas a change to $\Delta M \approx 0.07 M_{\odot}$ decreases the ^{56}Ni yield (C21.0OM models), displayed by heavy dashed lines in the bottom panel of Figure 4. In both cases the relative difference in the ^{56}Ni yields compared to the standard setup with $\Delta M = 0.05 M_{\odot}$ depends on t_{inj} and is largest for short t_{inj} and low ^{56}Ni production with the standard value of ΔM .

We notice again that this effect is considerably stronger if the nucleosynthesis in the heated mass ΔM itself is excluded from the ^{56}Ni budget (light-colored dashed lines in the bottom panel of Figure 4) instead of counting unbound matter in the energy-deposition layer also as ejecta (heavy dashed lines in the bottom panel of Figure 4). When ΔM is excluded from the ejecta, the ^{56}Ni yields in the $CM_{*}O$ (light-colored solid lines) and the $CM_{*}OM$ models (light-colored dashed lines) do not only become significantly lower but also very sensitive to the energy-injection timescale, as already mentioned in Section 4.3. This strong variation with t_{inj} in the case of our O-boundary models reminds one of the SM19 results with D-boundary, but the effect vanishes almost entirely for all

O-models when the ^{56}Ni production within the heated mass layer is added to the ejecta.

For completeness, we also tested a radical reduction of ΔM from our default of $0.05 M_{\odot}$ to the value of $0.005 M_{\odot}$ adopted by SM19 for the fixed mass in the energy-deposition layer (U- and C-models in Table 3 with M' as endings of their names). These simulations reproduce the trend witnessed for the C19.7OM models compared to the C19.7O models in the bottom panel of Figure 4, namely that a reduced ΔM tends to increase the ^{56}Ni production (see Figure 9). While the difference is small and thus has no relevant effect in the uncollapsed (and collapsed) models with the D-boundary (left panel of Figure 9) the increase is more significant in the simulations with O-boundary (right panel). However, considering all the results provided by Figures 4 and 9, one must conclude that, overall, the ^{56}Ni yields are not overly sensitive to the exact value chosen for ΔM , and that the corresponding variations are certainly secondary compared to the differences obtained between collapsed and uncollapsed models and between changing from D-boundary to O-boundary.

These findings shed light on the many ambiguities and the somewhat arbitrary choices that can be made in the treatments of artificial explosions with parametric methods. In any case, it is advisable to include also the mass of the energy-injection layer in the ejecta of the thermal bomb, if this matter gets ultimately expelled during the explosion. This is particularly relevant when the initial mass cut is assumed to be located at the more realistic $s/k_B = 4$ position and the thermal energy is dumped into an extended layer with mass ΔM , whose choice is inspired (roughly) by the mass heated by neutrinos in CCSNe. If otherwise the mass of ΔM is excluded from the ejecta, the ^{56}Ni production can become highly sensitive to the exact values of both ΔM and t_{inj} , depending on the density structure of the progenitor star.

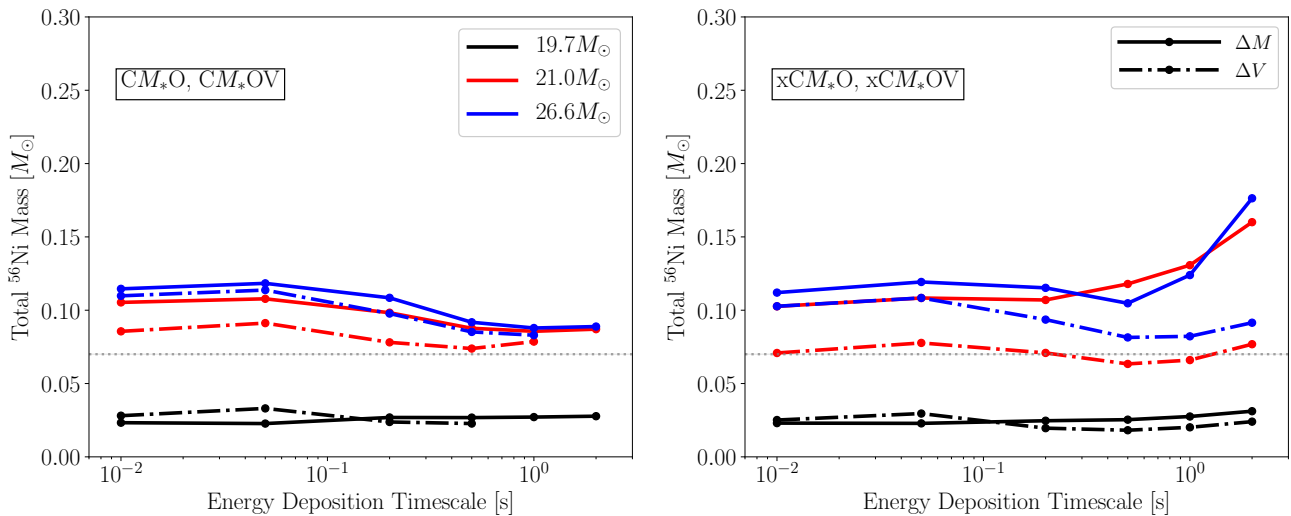


Figure 10. ^{56}Ni yields as functions of energy-injection timescale for collapsed CCSN models with fixed mass $\Delta M = 0.05 M_{\odot}$ (solid lines) and fixed volume (dash-dotted lines) of the energy-deposition layer. The left panel displays the results for our standard collapse to $r_{\min} = 500$ km, the right panel the cases with extreme collapse to $r_{\min} = 150$ km. The different colors correspond to the different progenitors as labelled in the left panel. Note that the models with fixed volume for the longest energy-deposition timescales in the left panel could not be finished because of the computational demands connected to small time steps. The horizontal grey dotted line indicates the ^{56}Ni yield of $0.07 M_{\odot}$ for a $\sim 10^{51}$ erg explosion, e.g., SN 1987A (Arnett et al. 1989).

4.5 Fixed volume for energy-injection layer

In another variation of the thermal-bomb modelling we also performed runs with fixed volume ΔV for the energy deposition, constrained to simulations including the collapse phase and applying the O-boundary (models $CM_{*}OV$ in Table 3). These simulations used the same volume for all of the three considered progenitors, and correspondingly the initial masses in the energy-injection volume were slightly different between these progenitors (Table 4). Moreover, these initial mass values were also different from the fixed masses ΔM in the heating layer of the $CM_{*}O$ models (except for the $26.6 M_{\odot}$ case), which we will compare the $CM_{*}OV$ models to. Although we found only a modest influence by variations of the fixed mass in the energy-deposition layer in Section 4.4, we will see that the moderate differences in the initial mass contained by the fixed heated volume can cause some subtle relative differences in the behavior of the simulations for different progenitor masses.

Our CCSN models with fixed volume for the energy-injection behave, overall, quite similarly to the models with fixed mass. This holds concerning the ^{56}Ni yields (left panel of Figure 10) as well as the explosion dynamics (left panels of Figure 11) and the peak-temperature distribution (left panels of Figure 12). However, the computation of the fixed ΔV -models is partly more difficult and more time consuming, because the time steps become small when the mass in the energy-deposition volume decreases and therefore the entropy per nucleon s increases. This implies a growth of the sound speed, because $c_s \approx \sqrt{(4/3) \cdot P/\rho} \propto \sqrt{(4/3) \cdot sT}$ for the radiation-dominated conditions in the heated volume, and therefore it leads to a corresponding reduction of the Courant-Friedrichs-Lewy limit for the length of the time steps. For this reason our $CM_{*}OV$ simulations with the longest energy-deposition timescales could partly not be fin-

ished due to their computational demands. Nevertheless, the available runs are sufficient to draw the essential conclusions.

In Figure 10, left panel, only minor differences in the ^{56}Ni production are visible between the $CM_{*}O$ models and the $CM_{*}OV$ models. Only the $21.0 M_{\odot}$ runs exhibit more sizeable differences, i.e., the $C21.0OV$ models eject systematically lower ^{56}Ni yields than the $C21.0O$ simulations, especially for short energy-injection times. The special role of the $C21.0OV$ models among the CCSN simulations for the three progenitors is explained by the fact that the initially heated mass in the $21.0 M_{\odot}$ models is the largest of all of the constant-volume models (see Table 4), whereas the heated volumes are the same for all cases. This implies that the heating rate per unit mass is smallest in the $C21.0OV$ models of the $21.0 M_{\odot}$ progenitor. In addition, the initial mass in the heated volume of the $C21.0OV$ models is also larger than the mass in the heating layer of the $C21.0O$ simulations ($0.068 M_{\odot}$ instead of $0.05 M_{\odot}$). For this reason the volume over which the heating is spread is greater in the $C21.0OV$ models, reducing the heating rate per volume in the innermost ejecta.

These differences have consequences for the shock strength. The shock in the $C21.0OV$ simulations is weaker and the peak temperatures remain lower than in the $C21.0O$ models (Figure 12, left panels), where the heated mass is not only smaller but the energy injection also occurs into a fixed mass and thus follows the expanding gas. In contrast, in the $C21.0OV$ simulations the heated gas expands out of the heated volume. For long heating timescales the energy injection into a fixed mass or a fixed volume makes little difference because the gas expands only slowly, allowing the infall of the preshock gas to proceed for a longer time, leading to higher kinetic energies and thus to stronger shock heating. Therefore the solid and dash-dotted lines in the left panel of Figure 10 approach each other for all progenitors when the heating timescales are long, consistent with the observation that the peak temperatures in the left panels of Figure 12 become very similar

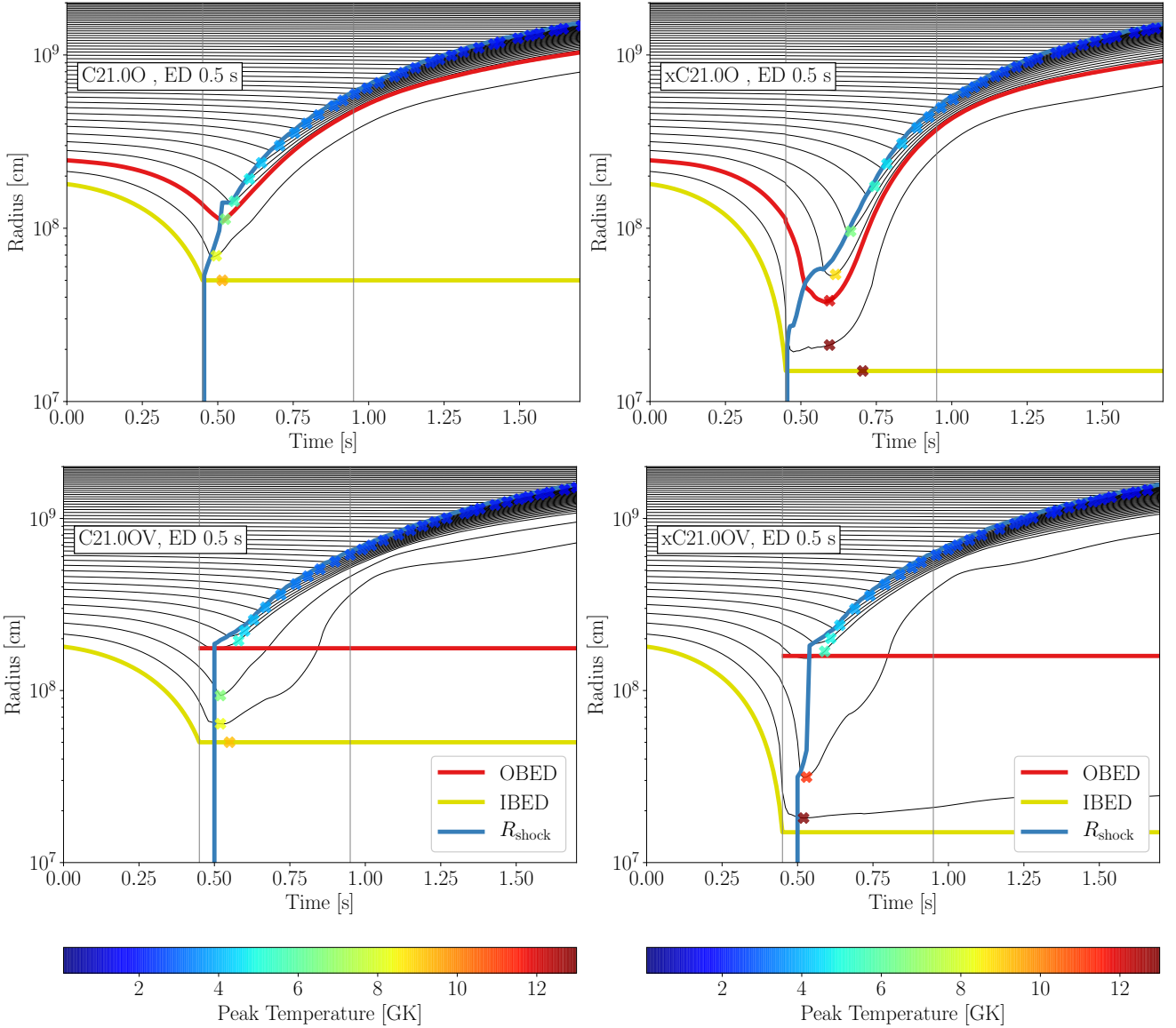


Figure 11. Radius evolution of Lagrangian mass shells versus time for CCSN runs of the $21 M_{\odot}$ progenitor with collapse phase and a representative energy-deposition timescale of 0.5 s; top left: for fixed mass of $\Delta M = 0.05 M_{\odot}$ in the energy-deposition layer and collapse to our default value for the minimum radius of $r_{\min} = 500$ km; top right: for the same fixed mass in the energy-deposition layer but collapse to $r_{\min} = 150$ km; bottom left: for fixed volume of the energy deposition and collapse to $r_{\min} = 500$ km; bottom right: for fixed energy-deposition volume and collapse to $r_{\min} = 150$ km. The thin black solid lines are the mass shells, spaced in steps of $0.025 M_{\odot}$, the blue line marks the shock radius, the yellow line the inner grid boundary, which is also the lower boundary of the energy-deposition layer, and the red line indicates the outer boundary of the energy-deposition layer, either at a fixed mass interval of $0.05 M_{\odot}$ above the inner boundary or at a fixed radius. Crosses indicate the instants when the peak temperature of each mass shell is reached; their colors correspond to temperature values as given by the color bars. Vertical lines mark the beginning and the end of the energy deposition.

for the higher values of t_{inj} . Instead, if the heating timescale is short, the heated gas in the $21.0 M_{\odot}$ models with fixed energy-deposition volume experiences lower heating rates per unit volume and moves out of the heated volume rather than receiving continuous energy input as in the C21.00 models, where the heating shifts outward with the expanding matter. Therefore the shock becomes weaker and the peak temperatures in particular of the innermost ejecta in the C21.00V simulations with short t_{inj} remain lower than in the C21.00 models. Since the initially heated mass in the C21.00V models is larger than in the fixed ΔV -simulations for the other

progenitors, this temperature effect and the correspondingly lower ^{56}Ni production are most pronounced in the C21.00V runs. A moderate opposite trend is visible for the C19.70V models with short t_{inj} because of the smallest value of the initial mass in the fixed heated volume in simulations with the $19 M_{\odot}$ progenitor (Table 4).

4.6 Effects of minimum radius for collapse

Finally, we also tested the influence of the minimum radius r_{\min} in the prescription of the initial collapse phase of

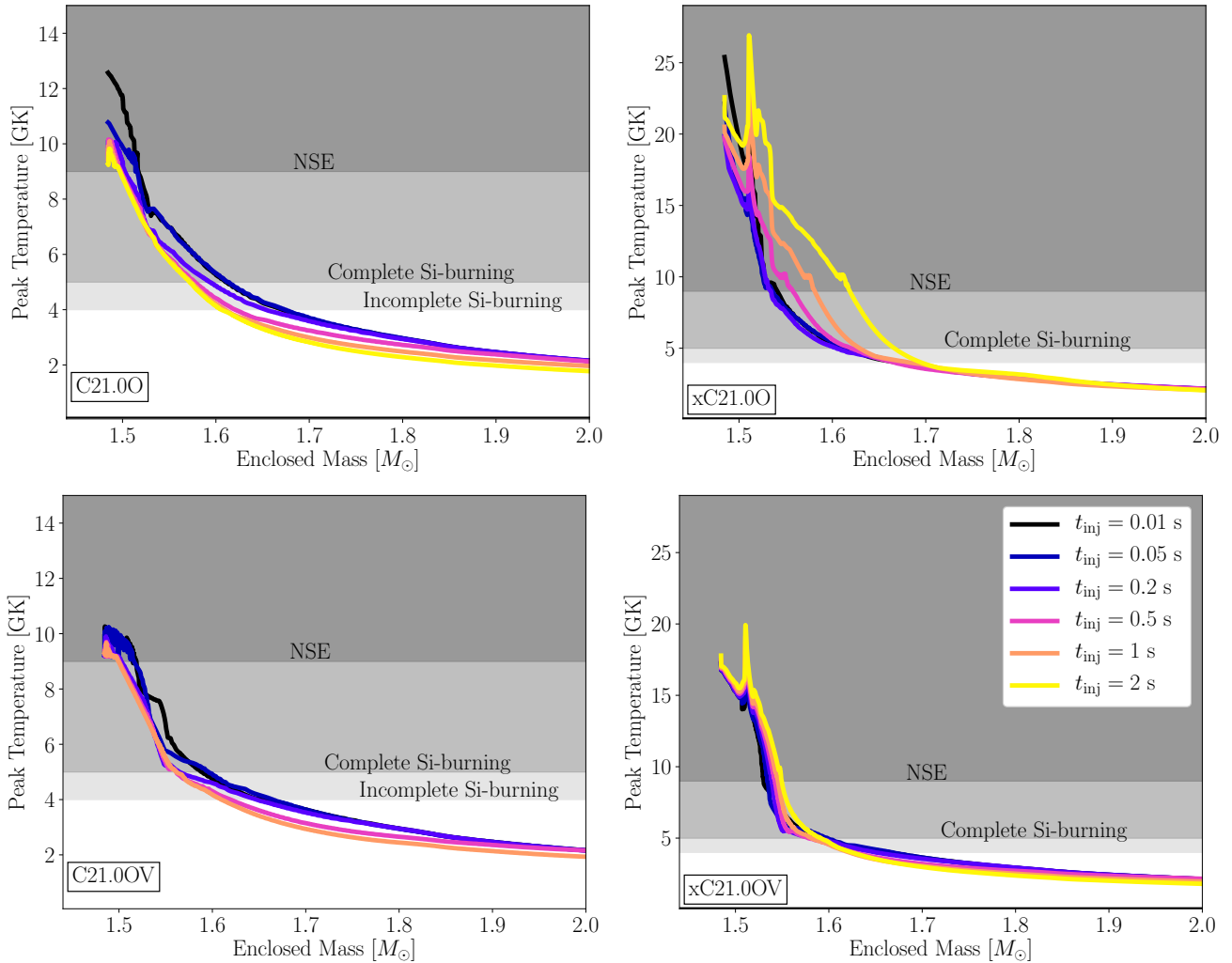


Figure 12. Peak temperatures as functions of enclosed mass for the CCSN runs with the $21 M_{\odot}$ progenitor and different energy-injection timescales for the same modelling setups shown in Figure 11; top left: for fixed mass of $\Delta M = 0.05 M_{\odot}$ in the energy-deposition layer and collapse to our default value for the minimum radius of $r_{\min} = 500$ km; top right: for the same fixed mass in the energy-deposition layer but collapse to $r_{\min} = 150$ km; bottom left: for fixed volume of the energy deposition and collapse to $r_{\min} = 500$ km; bottom right: for fixed energy-deposition volume and collapse to $r_{\min} = 150$ km. Different intensities of grey shading indicate different regimes of explosive nucleosynthesis as labelled.

the C-models by running thermal-bomb models with $r_{\min} = 150$ km, which is close to the radial location of the neutrino-heating layer in neutrino-driven explosion models, instead of our canonical choice of $r_{\min} = 500$ km. For doing these tests we constrained ourselves to the models with O-boundary for fixed mass layer ΔM (models $xCM_{*}O$ in Table 3) and fixed volume ΔV (models $xCM_{*}OV$ in Table 3) for the energy injection, and we will compare them with the default-collapse models of $CM_{*}O$ and $CM_{*}OV$. Here one has to keep in mind that all $CM_{*}O$ and $xCM_{*}O$ models, for all progenitors, were computed with exactly the same fixed mass of $\Delta M = 0.05 M_{\odot}$ for the energy-injection layer. The $CM_{*}OV$ and $xCM_{*}OV$ models for a given progenitor had effectively the same initial mass (up to the third digit) and nearly the same volume of the heated layer (Table 4). However, while the heated volume is the same in the CCSN runs for all progenitors, the initial masses in this volume differ between the three progenitors (Table 4).

Comparing the left and right panels of Figure 10, we witness only small differences in the ^{56}Ni production for short heating timescales between the $xCM_{*}O$ and the $CM_{*}O$ simulations, and also between the $xCM_{*}OV$ and the $CM_{*}OV$ simulations there are only relatively modest differences. The most prominent effect is a spreading between the ^{56}Ni yields of the $x\text{C}21.00$ and $\text{C}21.00\text{OV}$ models that is about twice as big as it is between the $\text{C}21.00$ and $\text{C}21.00\text{OV}$ cases (right panel of Figure 10). There is also a slightly greater gap between the yields of the $x\text{C}26.60$ and $\text{C}26.60\text{OV}$ simulations; this difference is again about double the size of that between the $\text{C}26.60$ and $\text{C}26.60\text{OV}$ models, where it is effectively insignificant. The reasons for the somewhat lower production of ^{56}Ni in the fixed-volume models with short energy-injection times were discussed in Section 4.5, and they lead to stronger effects in simulations with more extreme collapse.

For long heating timescales we observe an interesting, new phenomenon in the extreme-collapse models that is exactly

opposite to the pronounced decrease of the ^{56}Ni yields for longer t_{inj} in U-models reported by SM19 and reproduced by our calculations, and the similar but much weaker trends that one can spot in most of our C-models, too. Allowing for a deep collapse to $r_{\text{min}} = 150$ km we obtain increasing ^{56}Ni yields for longer energy-injection timescales in particular for the fixed- ΔM cases, but also, though less drastic, for the fixed- ΔV models (Figure 10, right panel). (It is possible that a mild version of this trend is also present in our default-collapse models with fixed heating volume, but unfortunately the corresponding simulations for long t_{inj} could not be finished.) The increase of the ^{56}Ni production for $t_{\text{inj}} = 1$ s and 2 s reverses the shallow decline that can be seen between $t_{\text{inj}} = 0.05$ s and 0.5 s.

The reason for this new effect can be inferred from the right panels of Figure 12. In stark contrast to all the other model sets plotted in Figure 5 and in the left panels of Figure 12, the extreme-collapse models with the longest energy-injection times tend to reach higher peak temperatures in a wider mass range than the corresponding simulations with short t_{inj} . This effect is particularly strong for the xC-models with fixed mass ΔM of the heating layer (upper right panel of Figure 12 for the CCSN runs with the $21.0 M_{\odot}$ progenitor). The mass-shell plots of Figure 11, right panels compared to the left panels, provide an explanation of this phenomenon. In the deep collapse cases, the matter is much more strongly compression-heated during the infall, and it also expands more slowly behind the shock than in the standard C-models. This effect is especially relevant when the heating timescales are long, because in such cases the shock accelerates outward less quickly, thus the gas ahead of the shock has more time to fall deeper into the gravitational potential of the newly formed neutron star, and when the outward moving shock sweeps up the infalling matter, the higher gas velocities lead to much stronger shock heating.

In the xC21.0OV and xC21.0O models there is an additional effect. In the fixed- ΔM models of the $21.0 M_{\odot}$ progenitor, the energy injection is initially constrained to a more narrow volume containing $0.05 M_{\odot}$, and it tracks the ejected matter. This leads to maximum peak temperatures in the mass shells well behind the shock (see upper right panel of Figure 11). In contrast, in the fixed- ΔV models of the same progenitor, the heated volume (initially containing $0.068 M_{\odot}$) is considerably larger than the initial heating volume in the corresponding fixed- ΔM models. Therefore the shock expansion reaches a larger radius within a shorter period of time, preventing the deep infall of the preshock material in the xC21.0-cases with fixed ΔV (compare upper and lower right panels of Figure 11). Consequently, the postshock heating is less extreme in the simulations with fixed energy-injection volume than in the models with fixed mass (see the upper and lower right panels of Figure 12).

In the extreme-collapse cases with fixed ΔV the heated volume is somewhat smaller than in the corresponding models with standard collapse because of smaller values of R_{IBED} and R_{OBED} (Table 4). Therefore the energy-deposition rate per volume in these xC-models is higher than in the C-models, and the innermost ejecta come from regions with stronger heating, for which reason also the xC-models with fixed ΔV exhibit a mild trend to higher postshock temperatures for long energy-injection timescales. Of course, the combined heating effect (compression by infall and shock, plus energy

injection) is significantly stronger when the heating follows the ejected mass in the xCM*O models, for which reason these models show a considerably steeper increase of the ^{56}Ni production with longer t_{inj} .

In contrast, for short heating timescales the explosion dynamics of models with default collapse and extreme collapse are quite similar and the differences in the peak-temperature distributions are mostly connected to the initially stronger compression heating in the xC-models. However, in both prescriptions of the collapse phase, similar amounts of mass are heated to NSE and complete Si-burning temperatures (compare the upper left with the upper right panel and the lower left with the lower right panel in Figure 12). Therefore the ^{56}Ni yields for short t_{inj} are similar between the C-models and the xC-models of each progenitor and both for fixed ΔM and for fixed ΔV , except for the effect that we already mentioned above, namely that the ^{56}Ni production in the xC21.0OV and xC26.6OV models compared to the xC21.0O and xC26.6O models is somewhat more reduced than in the C21.0OV and C26.6OV models relative to the C21.0O and C26.6O models (see the left and right panels of Figure 10).

By default our ^{56}Ni yields include nickel produced in the energy-deposition layer (see Section 3.1). In principle, one has to consider that some of this innermost matter may be unable to achieve escape conditions and thus may stay gravitationally bound, thus not contributing to the CCSN ejecta. From our model sets this issue affects especially the extreme-collapse cases with fixed volume for the energy injection, where the heated gas resides deep in the gravitational potential of the newly formed neutron star and the energy deposition does not follow the outward moving matter. Among these xC-models mainly the $21.0 M_{\odot}$ simulations are concerned, since the initial mass in the heated volume of these models is largest (see Table 4). One can see this in the lower right panel of Figure 11, because the innermost displayed mass shell exterior to R_{IBED} expands only very slowly there. The radial velocities of this shell over 30 s in the xC21.0OV simulations are only around 100 km s^{-1} and therefore considerably lower than the escape velocity, which is on the order of 1000 km s^{-1} at a radius of some 1000 km. Consequently, this matter might not become unbound despite its continuous, slow expansion until the end of our simulations. Subtracting the ^{56}Ni contained in this innermost material would somewhat reduce the nickel production, but such a correction would not mean a dominant effect for the xC21.0OV models. Nevertheless, it might damp the increase of the ^{56}Ni yields in these model runs for long energy-injection times seen in Figure 10, right panel.

5 SUMMARY AND DISCUSSION

The thermal bomb method is a widely used modelling approach to trigger CCSN explosions artificially by releasing energy into a chosen mass layer or chosen volume around a chosen location of the (initial, i.e. before fallback) mass cut, which usually coincides with the inner boundary of the computational grid. In the present paper we explored various dependencies of the thermal-bomb parameterization, in particular we considered models with and without an initial collapse phase, different timescales for the energy release, different radial positions of the mass cut, energy deposition in

a fixed mass layer or fixed volume, different masses for this layer, and different minimum radii for the contraction during the collapse phase. For this purpose we performed 1D CCSN simulations with the thermal-bomb method, using the PROMETHEUS-HOTB code, and we post-processed the ejecta for nucleosynthesis with the SkyNet open-source network. We focused here on the production of ^{56}Ni because of its pivotal importance for observational SN diagnostics. Moreover, the production of this dominant radioactive isotope can be considered as representative of the total output in iron-group and intermediate-mass nuclei without entering the discussion of yields of other isotopes, whose relative amounts are highly sensitive to the exact distribution of Y_e in the ejecta.

Our work was motivated by the recent finding of SM19, deduced from thermal-bomb simulations for three progenitors with different masses, that the production of $^{56,57}\text{Ni}$ and ^{44}Ti decreases dramatically for energy-injection timescales longer than about 100 ms. SM19 concluded that the production of these nuclear species and other elements is best compatible with observational constraints for nearly instantaneous explosions, i.e., for energy-release timescales of the thermal bomb as short as $\lesssim 50$ ms. If correct, this result would be a strong argument against the neutrino-driven explosion mechanism for CCSNe, because self-consistent ab initio simulations show that this mechanism provides the energy of the explosion only over timescales of seconds (see, e.g., [Bollig et al. 2021](#)).

In our simulations, mainly considering 19.7, 21.0, and $26.6 M_\odot$ progenitors with significantly different pre-collapse structures, we confirmed the results obtained by SM19, namely a strong anti-correlation between ^{56}Ni yields and energy-injection timescale. However, we obtained these results only when the thermal bomb was assumed to release its energy in the uncollapsed progenitor models. Including an initial collapse phase, which is the more realistic approach when stellar core collapse, neutron star formation, and CCSN explosions are supposed to be simulated, the trend witnessed by SM19 effectively disappears and the ^{56}Ni production becomes almost independent of the timescale for the energy release. Allowing for an initial collapse to a minimal radius of 150 km instead of our default value of 500 km, thus more closely adopting conditions similar to those in neutrino-driven explosions, we even obtained a reversal of the trend seen in uncollapsed models. In such calculations with the more extreme collapse, we found that long energy-injection timescales, especially when longer than ~ 1 s, lead to a higher production of ^{56}Ni than the shorter energy-deposition times, which trigger more rapid explosions.

Therefore there is no reason to conclude on grounds of thermal-bomb simulations that the ^{56}Ni production in slow explosions as expected for the neutrino-driven mechanism is in conflict with observational data. The result reported by SM19 for their thermal-bomb explosions of uncollapsed progenitor models was caused by the energy injection into the low-density, hydrostatic stellar profiles, which permits easy expansion of the ejecta with corresponding expansion-cooling as soon as the energy release is switched on. Therefore only small amounts of matter close to the heated mass shell (i.e., the defined mass cut) can reach temperatures that are sufficiently high for NSE and Si-burning. The conditions for such temperatures are strongly disfavored for longer energy-injection timescales. In contrast, when an initial collapse phase is included in the thermal-bomb modelling, the energy

deposition occurs in infalling matter, which expands much less readily, because the SN shock wave needs to propagate outward against the ram pressure of infalling stellar layers. In this case it has to receive more energy input for a predefined value of the final explosion energy, and the correspondingly stronger explosion shock can heat more mass to NSE and Si-burning conditions.

Varying the different inputs for the parametric description of the thermal bombs for a fixed value of the explosion energy, we found that the most sensitive aspects for the production of ^{56}Ni are the inclusion of the initial collapse instead of releasing the energy into the uncollapsed progenitor, and the location of the initial mass cut at the radius where the entropy per nucleon reaches $s/k_B = 4$ instead of the position where $Y_e = 0.48$. There is only a relatively modest influence of the exact value of the fixed mass ΔM in the energy-deposition layer. Also the choice of a fixed volume for the energy release instead of a fixed mass causes only secondary differences. Once the initial collapse is included, also the timescale of the energy release by the thermal bomb leads to variations only on a secondary level. For the more realistic choice of the initial mass cut at $s/k_B = 4$, which can be better motivated by neutrino-driven explosion models, it is crucial to also include matter in the heated layer in the ejecta, if this matter becomes unbound during the explosion.

Because of their numerous degrees of freedom, thermal-bomb models can certainly not be employed to assess the viability of any kind of physical explosion mechanism. For example, artificial explosion methods like the thermal bombs can hardly be expected to reproduce the dynamics of neutrino-driven explosions in a physically correct and reliable way. In particular, fixing the mass layer for the energy injection means that the energy input follows the expanding matter, which is unrealistic. Fixing instead the volume for the energy release either overestimates the heated volume or underestimates the heated mass in this heated volume, where in addition the mass decreases with time, which again is not a realistic description of the neutrino-driven mechanism. Fortunately, the ^{56}Ni production of thermal bomb simulations that include a collapse phase turned out not to be overly sensitive to such alternative choices.

Thermal bombs are a numerical recipe that depends on a variety of parameterized inputs that need to be defined. Nevertheless, even with the best choice of these inputs, their usefulness for quantitative predictions of iron-group and intermediate-mass-element nucleosynthesis will always be hampered by the unknown value of the explosion energy and, in principle, also of the initial mass cut. Moreover, iron-group species such as the isotopes of $^{56,57}\text{Ni}$ and of ^{44}Ti are formed in ejecta whose Y_e evolves due to weak-force interactions of neutrinos and where multi-dimensional flows play a crucial role. None of these are taken into account in a simple thermal-bomb treatment. Therefore the best one can expect of any artificial explosion trigger is that the method should be set up such that it does not massively overproduce or underproduce nickel and it should also be set up such that the correct trends of the ^{56}Ni production with explosion energy, explosion time scale, and progenitor structure can be maintained.

Since thermal bombs provide an easy-to-apply recipe to trigger explosions, it is very likely that they will remain in use as a method of choice for the exploration of CCSN nu-

cleosynthesis, for example in large sets of progenitor models, despite all the mentioned caveats (e.g. Farmer et al. 2021). In view of the results of our study, we recommend the following prescriptions:

(i) Include a collapse phase before the energy release of the thermal bomb is started. A minimum collapse radius near 500 km seems to be sufficient and is computationally less demanding than a smaller radius.

(ii) Since self-consistent simulations of neutrino-driven CCSNe show that the explosion sets in when the infalling Si/O interface reaches the stagnant bounce shock, the initial mass cut should be chosen near the $s/k_B = 4$ location instead of putting it close to the edge of the iron core. Therefore Y_e in the layer of energy injection by the thermal bomb is very close to 0.5 (typically higher than 0.497).

(iii) For this reason ^{56}Ni will be efficiently produced in the energy-injection layer and the matter in this layer should be included in the ejecta, if it becomes gravitationally unbound by the explosion.

(iv) Using a fixed mass layer ΔM for the energy injection is numerically easier than a fixed volume, and both choices do not cause any major differences. The exact value of ΔM is not crucial. We suggest $0.05 M_\odot$, but smaller masses lead to very similar nickel yields.

(v) With the recommended setup the ^{56}Ni production is basically insensitive to the timescale chosen for the energy injection by the thermal bomb.

Of course, these recommendations are based on a small set of simulations for only three progenitors and a defined explosion energy of 10^{51} erg in all of our thermal-bomb calculations. A wider exploration is desirable to test the more general reliability of our proposed parameter settings. Beyond the prescriptions listed above, the value of the explosion energy is another crucial input into the thermal-bomb modelling. Its specification has to be guided by our first-principle understanding of the physics of the CCSN mechanism in stars of different masses. In future work we plan to compare thermal-bomb models and direct simulations of neutrino-driven CCSN explosions with respect to the progenitor and explosion energy dependent production of ^{56}Ni and other iron-group and intermediate-mass elements.

ACKNOWLEDGEMENTS

We are grateful to Thomas Ertl for his assistance in the starting phase of the project and thank Ewald Müller and Johannes Ringler for discussions. Support by the Deutsche Forschungsgemeinschaft (DFG, German Research Foundation) through Sonderforschungsbereich (Collaborative Research Center) SFB-1258 “Neutrinos and Dark Matter in Astro- and Particle Physics (NDM)” and under Germany’s Excellence Strategy through Cluster of Excellence ORIGINS (EXC-2094)-390783311 is acknowledged.

DATA AVAILABILITY

The data of our calculations will be made available upon reasonable request.

SOFTWARE

PROMETHEUS-HOTB (Janka & Müller 1996; Kifonidis et al. 2003; Scheck et al. 2006; Arcones et al. 2007; Ugliano et al. 2012; Ertl et al. 2016); KEPLER (Weaver et al. 1978); SkyNet (Lippuner & Roberts 2017); Matplotlib (Hunter 2007); NumPy (van der Walt et al. 2011).

REFERENCES

- Abbott R., et al., 2021, *ApJ*, **913**, L7
- Aguilera-Dena D. R., Müller B., Antoniadis J., Langer N., Dessart L., Vigna-Gómez A., Yoon S.-C., 2022, arXiv e-prints, p. [arXiv:2204.00025](https://arxiv.org/abs/2204.00025)
- Aloy M. A., Müller E., Ibáñez J. M., Martí J. M., MacFadyen A., 2000, *ApJ*, **531**, L119
- Arcones A., Janka H. T., Scheck L., 2007, *A&A*, **467**, 1227
- Arnett W. D., Bahcall J. N., Kirshner R. P., Woosley S. E., 1989, *ARA&A*, **27**, 629
- Aufferheide M. B., Baron E., Thielemann F. K., 1991, *ApJ*, **370**, 630
- Barker B. L., Harris C. E., Warren M. L., O’Connor E. P., Couch S. M., 2022, *ApJ*, **934**, 67
- Bersten M. C., Benvenuto O., Hamuy M., 2011, *ApJ*, **729**, 61
- Bollig R., Yadav N., Kresse D., Janka H.-T., Müller B., Heger A., 2021, *ApJ*, **915**, 28
- Bruenn S. W., et al., 2016, *ApJ*, **818**, 123
- Burrows A., Vartanyan D., 2021, *Nature*, **589**, 29
- Chieffi A., Limongi M., 2013, *ApJ*, **764**, 21
- Couch S. M., 2017, *Philosophical Transactions of the Royal Society of London Series A*, **375**, 20160271
- Couch S. M., Warren M. L., O’Connor E. P., 2020, *ApJ*, **890**, 127
- Cowan J. J., Sneden C., Lawler J. E., Aprahamian A., Wiescher M., Langanke K., Martínez-Pinedo G., Thielemann F.-K., 2021, *Reviews of Modern Physics*, **93**, 015002
- Curtis S., Ebinger K., Fröhlich C., Hempel M., Perego A., Liebendörfer M., Thielemann F.-K., 2019, *ApJ*, **870**, 2
- Curtis S., Wolfe N., Fröhlich C., Miller J. M., Wollaeger R., Ebinger K., 2021, *ApJ*, **921**, 143
- Dessart L., Hillier D. J., Sukhbold T., Woosley S. E., Janka H. T., 2021a, *A&A*, **652**, A64
- Dessart L., Hillier D. J., Sukhbold T., Woosley S. E., Janka H. T., 2021b, *A&A*, **656**, A61
- Diehl R., et al., 2021, *Publ. Astron. Soc. Australia*, **38**, e062
- Ebinger K., Curtis S., Fröhlich C., Hempel M., Perego A., Liebendörfer M., Thielemann F.-K., 2019, *ApJ*, **870**, 1
- Ebinger K., Curtis S., Ghosh S., Fröhlich C., Hempel M., Perego A., Liebendörfer M., Thielemann F.-K., 2020, *ApJ*, **888**, 91
- Ertl T., Janka H. T., Woosley S. E., Sukhbold T., Ugliano M., 2016, *ApJ*, **818**, 124
- Ertl T., Woosley S. E., Sukhbold T., Janka H. T., 2020, *ApJ*, **890**, 51
- Farmer R., Laplace E., de Mink S. E., Justham S., 2021, *ApJ*, **923**, 214
- Hashimoto M., Nomoto K., Shigeyama T., 1989, *A&A*, **210**, L5
- Hayden M. R., et al., 2015, *ApJ*, **808**, 132
- Hix W. R., et al., 2014, *AIP Advances*, **4**, 041013
- Hunter J. D., 2007, *Computing in Science and Engineering*, **9**, 90
- Iwamoto K., Nomoto K., Höflich P., Yamaoka H., Kumagai S., Shigeyama T., 1994, *ApJ*, **437**, L115
- Janka H.-T., 2012, *Annual Review of Nuclear and Particle Science*, **62**, 407
- Janka H. T., Müller E., 1996, *A&A*, **306**, 167
- Janka H. T., Langanke K., Marek A., Martínez-Pinedo G., Müller B., 2007, *Phys. Rep.*, **442**, 38
- Janka H.-T., Melson T., Summa A., 2016, *Annual Review of Nuclear and Particle Science*, **66**, 341

- Jerkstrand A., et al., 2015, *ApJ*, **807**, 110
- Khokhlov A. M., Höflich P. A., Oran E. S., Wheeler J. C., Wang L., Chtchelkanova A. Y., 1999, *ApJ*, **524**, L107
- Kifonidis K., Plewa T., Janka H. T., Müller E., 2000, *ApJ*, **531**, L123
- Kifonidis K., Plewa T., Müller E., 2001, in Arnould M., Lewitowicz M., Oganessian Y. T., Akimune H., Ohta M., Utsunomiya H., Wada T., Yamagata T., eds, American Institute of Physics Conference Series Vol. 561, Symposium on Nuclear Physics IV. pp 21–32 ([arXiv:astro-ph/0011206](https://arxiv.org/abs/astro-ph/0011206)), doi:10.1063/1.1372778
- Kifonidis K., Plewa T., Janka H. T., Müller E., 2003, *A&A*, **408**, 621
- Kifonidis K., Plewa T., Scheck L., Janka H. T., Müller E., 2006, *A&A*, **453**, 661
- Kobayashi C., Karakas A. I., Lugaro M., 2020, *ApJ*, **900**, 179
- Limongi M., Chieffi A., 2003, *ApJ*, **592**, 404
- Limongi M., Chieffi A., 2006, *ApJ*, **647**, 483
- Limongi M., Chieffi A., 2012, *ApJS*, **199**, 38
- Limongi M., Chieffi A., 2018, *ApJS*, **237**, 13
- Lippuner J., Roberts L. F., 2017, *ApJS*, **233**, 18
- MacFadyen A. I., Woosley S. E., 1999, *ApJ*, **524**, 262
- Maeda K., Nomoto K., 2003, *ApJ*, **598**, 1163
- Matteucci F., 2003, *Ap&SS*, **284**, 539
- Meskhi M. M., Wolfe N. E., Dai Z., Fröhlich C., Miller J. M., Wong R. K. W., Vilalta R., 2022, *ApJ*, **932**, L3
- Mezzacappa A., 2005, *Annual Review of Nuclear and Particle Science*, **55**, 467
- Moriya T., Tominaga N., Tanaka M., Nomoto K., Sauer D. N., Mazzali P. A., Maeda K., Suzuki T., 2010, *ApJ*, **719**, 1445
- Morozova V., Piro A. L., Renzo M., Ott C. D., Clausen D., Couch S. M., Ellis J., Roberts L. F., 2015, *ApJ*, **814**, 63
- Müller E., 1986, *A&A*, **162**, 103
- Müller B., 2016, *Publ. Astron. Soc. Australia*, **33**, e048
- Müller B., 2020, *Living Reviews in Computational Astrophysics*, **6**, 3
- Müller B., Heger A., Liptai D., Cameron J. B., 2016, *MNRAS*, **460**, 742
- Müller B., Melson T., Heger A., Janka H.-T., 2017a, *MNRAS*, **472**, 491
- Müller T., Prieto J. L., Pejcha O., Clocchiatti A., 2017b, *ApJ*, **841**, 127
- Nagataki S., Hashimoto M.-a., Sato K., Yamada S., 1997, *ApJ*, **486**, 1026
- Nagataki S., Mizuta A., Yamada S., Takabe H., Sato K., 2003, *ApJ*, **596**, 401
- Nagataki S., Mizuta A., Sato K., 2006, *ApJ*, **647**, 1255
- Nakamura T., Umeda H., Iwamoto K., Nomoto K., Hashimoto M.-a., Hix W. R., Thielemann F.-K., 2001, *ApJ*, **555**, 880
- Nomoto K., Tominaga N., Umeda H., Kobayashi C., Maeda K., 2006, *Nuclear Phys. A*, **777**, 424
- O'Connor E., Ott C. D., 2011, *ApJ*, **730**, 70
- Ono M., Nagataki S., Ferrand G., Takahashi K., Umeda H., Yoshida T., Orlando S., Miceli M., 2020, *ApJ*, **888**, 111
- Orlando S., et al., 2020, *A&A*, **636**, A22
- Paxton B., Bildsten L., Dotter A., Herwig F., Lesaffre P., Timmes F., 2011, *ApJS*, **192**, 3
- Paxton B., et al., 2015, *ApJS*, **220**, 15
- Pejcha O., Thompson T. A., 2015, *ApJ*, **801**, 90
- Perego A., Hempel M., Fröhlich C., Ebinger K., Eichler M., Casanova J., Liebendörfer M., Thielemann F. K., 2015, *ApJ*, **806**, 275
- Ricks W., Dwarkadas V. V., 2019, *ApJ*, **880**, 59
- Sandoval M. A., Hix W. R., Messer O. E. B., Lentz E. J., Harris J. A., 2021, *ApJ*, **921**, 113
- Sawada R., Maeda K., 2019, *ApJ*, **886**, 47
- Scheck L., Kifonidis K., Janka H.-T., Müller E., 2006, *A&A*, **457**, 963
- Schneider F. R. N., Podsiadlowski P., Müller B., 2021, *A&A*, **645**, A5
- Shigeyama T., Nomoto K., Hashimoto M., 1988, *A&A*, **196**, 141
- Shimizu T. M., Ebisuzaki T., Sato K., Yamada S., 2001, *ApJ*, **552**, 756
- Siegel D. M., Barnes J., Metzger B. D., 2019, *Nature*, **569**, 241
- Sukhbold T., Woosley S. E., 2014, *ApJ*, **783**, 10
- Sukhbold T., Ertl T., Woosley S. E., Brown J. M., Janka H. T., 2016, *ApJ*, **821**, 38
- Suwa Y., Tominaga N., Maeda K., 2019, *MNRAS*, **483**, 3607
- The LIGO Scientific Collaboration et al., 2021, arXiv e-prints, p. [arXiv:2111.03606](https://arxiv.org/abs/2111.03606)
- Thielemann F.-K., Hashimoto M.-A., Nomoto K., 1990, *ApJ*, **349**, 222
- Thielemann F.-K., Nomoto K., Hashimoto M.-A., 1996, *ApJ*, **460**, 408
- Timmes F. X., Woosley S. E., Weaver T. A., 1995, *ApJS*, **98**, 617
- Ugliano M., Janka H.-T., Marek A., Arcones A., 2012, *ApJ*, **757**, 69
- Umeda H., Nomoto K., 2008, *ApJ*, **673**, 1014
- Valerin G., et al., 2022, *MNRAS*, **513**, 4983
- Weaver T. A., Zimmerman G. B., Woosley S. E., 1978, *ApJ*, **225**, 1021
- Wirth H., Jerabkova T., Yan Z., Kroupa P., Haas J., Šubr L., 2021, *MNRAS*, **506**, 4131
- Wongwathanarat A., Janka H.-T., Müller E., 2010, *ApJ*, **725**, L106
- Wongwathanarat A., Janka H. T., Müller E., 2013, *A&A*, **552**, A126
- Wongwathanarat A., Müller E., Janka H. T., 2015, *A&A*, **577**, A48
- Wongwathanarat A., Janka H.-T., Müller E., Pllumbi E., Wanajo S., 2017, *ApJ*, **842**, 13
- Woosley S. E., 1988, *ApJ*, **330**, 218
- Woosley S. E., Heger A., 2007, *Phys. Rep.*, **442**, 269
- Woosley S. E., Hoffman R. D., 1992, *ApJ*, **395**, 202
- Woosley S., Janka T., 2005, *Nature Physics*, **1**, 147
- Woosley S. E., Weaver T. A., 1995, *ApJS*, **101**, 181
- Woosley S. E., Heger A., Weaver T. A., 2002, *Reviews of Modern Physics*, **74**, 1015
- Woosley S. E., Sukhbold T., Janka H. T., 2020, *ApJ*, **896**, 56
- Yamamoto Y., Fujimoto S.-i., Nagakura H., Yamada S., 2013, *ApJ*, **771**, 27
- Yang S., et al., 2021, *A&A*, **655**, A90
- Young P. A., Fryer C. L., 2007, *ApJ*, **664**, 1033
- Zhang W., Woosley S. E., Heger A., 2008, *ApJ*, **679**, 639
- van der Walt S., Colbert S. C., Varoquaux G., 2011, *Computing in Science and Engineering*, **13**, 22

This paper has been typeset from a $\text{\TeX}/\text{\LaTeX}$ file prepared by the author.